TECHNISCHE UNIVERSITÄT WIEN
Vienna University of Technology

DIPLOMARBEIT

Optical conductivity in the Falicov-Kimball model: a dual fermion perspective

zur Erlangung des akademischen Grades

Diplom-Ingenieurin

im Rahmen des Studiums

Technische Physik

eingereicht von

Katharina Astleithner
Matrikelnummer 01255384

ausgeführt am Institut für Festkörperphysik
der Fakultät für Physik der Technischen Universität Wien

Betreuung
Betreuer: Prof. Dr. Karsten Held
Mitwirkung: Dr. Tin Ribic
Dr. Anna Kauch

Wien, 02.04.2019

(Unterschrift Verfasser) (Unterschrift Betreuer)

Abstract

The Falicov-Kimball model (FKM) is one of the simplest models to describe correlation effects in solid systems. It can be solved semi-analytically in dynamical mean field theory (DMFT), where all purely local correlations between electrons are taken into account and therefore within DMFT a good description of phenomena such as the metal-to-insulator transition is obtained. However, the charge density wave fluctuations that dominate the physics of the FKM and lead to a phase transition into an ordered state emerge from nonlocal correlations. To include such nonlocal correlations, diagrammatic extensions of DMFT have been developed recently. One of these methods, the dual fermion (DF) approach, is employed in this thesis to analyze the effect of nonlocal correlations. Especially, the effect of such nonlocal vertex corrections onto the optical conductivity – describing the interaction of light with the system – is investigated. It is shown that besides well-known phenomena, such as weak localization, a new form of bosonic optical excitations, coined π-tons, is prevalent in the FKM.

Zusammenfassung

Das Falicov-Kimball Modell (FKM) ist eines der einfachsten Modelle zur Beschreibung von Korrelationen in Festkörpersystemen. Es kann im Rahmen der dynamischen Molekularfeldtheorie (DMFT) semi-analytisch gelöst werden. Die DMFT berücksichtigt alle rein lokalen Korrelationen zwischen den Elektronen und liefert daher eine gute Beschreibung von Phänomenen wie dem Metall-Isolator-Übergang. Allerdings stammen die Ladungsdichtewellenfluktuationen, die im FKM vorherrschen und zu einem Phasenübergang in einen geordneten Zustand führen, von nichtlokalen Korrelationen. Um solche nicht-lokalen Korrelationen ebenfalls zu berücksichtigen, sind in den letzten Jahren diagrammatische Erweiterungen von DMFT entwickelt worden. Eine solche Methode, der Ansatz der dualen Fermionen (DF), wird in dieser Arbeit verwendet, um die Effekte von nichtlokalen Korrelationen zu analysieren. Insbesondere wird der Einfluss von solchen nichtlokalen Vertexkorrekturen auf die optische Leitfähigkeit untersucht, die die Wechselwirkung des Systems mit Licht beschreibt. Es wird gezeigt, dass neben bekannten Phänomenen wie der schwachen Lokalisierung eine neue Form von bosonischen optischen Anregungen, sogenannte π-tonen, im FKM vorherrscht.

Contents

1 Introduction

The goal of solid state physics is to find a proper description of the different properties of a wide variety of materials. The particular difficulty is that a solid consists of a huge number of particles interacting with each other, making it impossible to find an exact analytical solution for this problem. Consequently, many different approaches in many-body physics have been considered throughout the last decades to tackle this problem. One such approach is density functional theory (DFT) [1], which successfully describes materials with weak correlations. This is the case for systems with s- or p-bands, where the Coulomb repulsion between electrons is screened rather well. However, in materials with partially filled d- and f-orbitals, electrons are more localized, leading to strong correlations which in turn are the origin for many interesting phenomena such as the Mott-Hubbard metal-to-insulator transition [2] or high-temperature superconductivity in cuprates [3]. The basic physics of these strongly correlated systems is characterized in most cases by two competing terms: a local interaction between electrons on the one hand and their movement between lattice sites on the other hand. In this regard, the Hubbard [4] and the Falicov-Kimball model [5] are two simplified models describing correlated systems. Despite their simplicity, finding an exact solution remains an enormous challenge. Taking only local correlations into account, dynamical mean field theory (DMFT) [6] has proven to be a successful method for describing systems where this local part of correlations is most relevant. DMFT however fails to describe systems where nonlocal correlations are important, which applies to low-dimensional systems or near phase-transitions. In order to go beyond DMFT by considering also nonlocal correlations in addition, diagrammatic extensions of DMFT have been developed in recent years, the dynamical vertex approximation (DΓA) [7] and the dual fermion approach (DF) [8] being mentioned here.

In this thesis, the DF approach using the complete parquet equations is employed for the Falicov-Kimball model (FKM) on a square lattice. This approach captures the physics originating from nonlocal correlations and extends the purely local DMFT results for the FKM. The necessary methods for this purpose and the FKM itself are introduced in chapter 2, including the basic formalism of Green's functions, the parquet equations and a description of DMFT and the DF approach.

In chapter 3 the actual implementation of the DF approach for the FKM associated with the parquet equations is discussed. This is followed by corresponding results for the self-energy, Green's function and physical susceptibilities, both for a half-filled system and a system with low electron occupation. This full parquet calculation is then compared to a ladder DF

approximation in chapter 4, where again first the implementation and then corresponding results are presented.

Based on the parquet and ladder results, the optical conductivity is calculated, showing insight to the interaction of light with the system. In the full parquet calculation, the different contributions to the full vertex corrections of the conductivity are analyzed. It is found that it is the contribution of the $\overline{ph}$-channel that is prevalent in the FKM, and the by far largest contribution stems from a relative momentum $\vec{k}' - \vec{k} = (\pi, \pi)$, which can be associated with a specific new type of optical excitation, coined π-ton [9]. This is discussed in full detail in chapter 5. In addition, results stemming from a pp-ladder approximation are investigated, confirming that these diagrams are responsible for weak localization in the system.

Finally, the main aspects of the thesis are revisited in the conclusion in chapter 6.

2 Methods and Model

2.1 Green's functions

Green's functions are the most essential tool for describing many-body systems. Instead of looking at the behavior of every single electron and calculating the corresponding wave function, we are rather interested in single excitations as a response to external perturbations, as they determine physical quantities such as the optical conductivity or susceptibilities. We start from an occupied state, and introduce a formalism where individual electrons are added to or removed from this state. This can be achieved in second quantization by the field operators $c_i^\dagger(t)$ and $c_i(t)$, creating or annihilating a particle at time t, the index i indicating the degrees of freedom of the system, such as lattice site or momentum and spin.

To describe this situation, the one-particle causal Green's function is introduced. It is defined as [10]

$$G_{ij}(t'', t') := -i\langle \mathcal{T} c_i(t'') c_j^\dagger(t') \rangle. \tag{2.1}$$

Here, $\mathcal{T}$ denotes the Wick time-ordering operator which orders the operators following after it according to their time, i.e. the operators of a later time are always to the left of the ones of an earlier time. The averaging is done by using the density operator ρ of the system for the grand canonical ensemble, so the average of an operator $\mathcal{A}$ is defined by $\langle \mathcal{A} \rangle = \frac{tr(\rho \mathcal{A})}{tr(\rho)}$, where $tr(...)$ indicates the trace over a full basis of the Fock space. Basically, the Green's function describes a process, where in one case ($t'' > t'$) a particle is added to our system and propagates from (j, t') to (i, t'') and in the other case ($t' > t''$) a particle is removed and the resulting hole propagates from (i, t'') to (j, t').

To account for the analogy between the time evolution operator $U(t) = e^{-iHt}$ for a system with a given Hamilton operator H and the statistical density operator $\rho = e^{-\beta H}$ ($\beta = 1/T$ being the inverse temperature) the so-called temperature Green's function is introduced by performing a Wick rotation to imaginary time τ, $t \to -i\tau$. It depends only on the difference between two times $\tau = \tau'' - \tau'$, so it is written as

$$G_{ij}(\tau) \equiv G_{ij}(\tau, 0) = -\langle \mathcal{T} e^{-H(\beta - \tau)} c_i e^{-H\tau} c_j^\dagger \rangle. \tag{2.2}$$

The temperature Green's function shows a cyclic property for $-\beta \leq \tau \leq \beta$:

$$G_{ij}(\tau - \beta) = \mp G_{ij}(\tau), \tag{2.3}$$

where the minus sign corresponds to fermions and the plus sign for bosons, so temperature Green's functions are periodic for bosons and antiperiodic for fermions. Due to this property there are only discrete Fourier components, at the so-called Matsubara frequencies:

$$\nu_n = (2n+1)\frac{\pi}{\beta} \qquad \text{for fermions,} \tag{2.4}$$

$$\omega_n = 2n\frac{\pi}{\beta} \qquad \text{for bosons.} \tag{2.5}$$

The Fourier transformation of the Green's function is then given by

$$G_{ij}(\nu_n) = \int_0^\beta d\tau e^{i\nu_n \tau} G_{ij}(\tau), \tag{2.6}$$

$$G_{ij}(\tau) = \frac{1}{\beta} \sum_{\nu_n} e^{-i\nu_n \tau} G_{ij}(\nu_n). \tag{2.7}$$

Now we want to take into consideration the interaction U between two particles. To this end, we consider the perturbation theory series and perform an expansion around the noninteracting case $U = 0$. This corresponds to the technique of Feynman diagrams, as described for example in [10]. In this formalism, the Fourier transformed unperturbed Green's function $G_0(\vec{k}, \nu)$ is denoted by a dashed line and the interaction U by a wiggled line, as shown in Fig. 2.1. Any arbitrary Feynman diagram can be built out of these two elements.

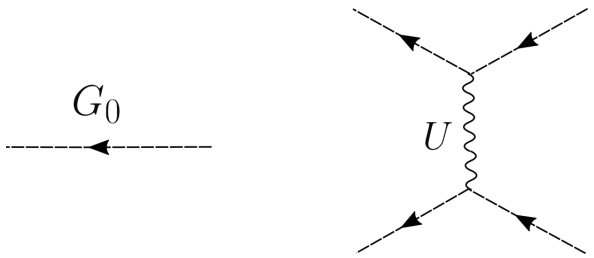

Figure 2.1 – In the formalism of Feynman diagrams, the unperturbed one-particle Green's function $G_0(\vec{k}, \nu)$ is drawn as a dashed line (left), the interaction U between two particles as a wiggled line (right).

The self-energy $\Sigma(\vec{k},\nu)$ is defined as the sum of all topologically distinct one-particle irreducible diagrams with an amputated incoming and outgoing leg, some of which are shown in Fig. 2.2. A diagram is called *one-particle irreducible*, if it cannot be separated into two parts by cutting one internal Green's function G_0 line. Σ is connected to the full interacting Green's function $G(\vec{k},\nu)$ via the Dyson equation, diagrammatically shown in Fig. 2.3:

$$G(\vec{k},\nu) = G_0(\vec{k},\nu) + G_0(\vec{k},\nu)\Sigma(\vec{k},\nu)G(\vec{k},\nu). \tag{2.8}$$

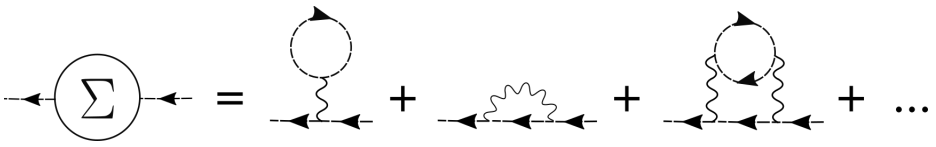

Figure 2.2 – The sum of all one-particle irreducible diagrams gives the self-energy $\Sigma(\vec{k},\nu)$. Here only the first three diagrams are shown. Note that the self-energy is defined without the outer legs drawn here.

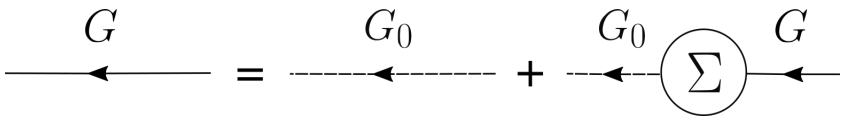

Figure 2.3 – The Dyson equation connects the interacting Green's function $G(\vec{k},\nu)$, denoted by a full line, with the unperturbed Green's function $G_0(\vec{k},\nu)$, denoted by a dashed line, and the self-energy $\Sigma(\vec{k},\nu)$.

So far the one-particle Green's function was regarded. The next step is to consider two-particle Green's functions, describing two elementary excitations in the many-body background, which are defined analogously to (2.1) in imaginary time,

$$G^{(2)}_{ijkl}(\tau_1,\tau_2,\tau_3) = -\langle \mathcal{T} c_i(\tau_1) c_j^\dagger(\tau_2) c_k(\tau_3) c_l^\dagger(0)\rangle. \tag{2.9}$$

This thermal average can be separated into an independent disconnected part, consisting of the simple product of one-particle Green's functions, and a connected part, associated with the scattering amplitude between two particles and represented by the full vertex function F. This is illustrated in Fig. 2.4 and is written in Matsubara frequency and momentum space as

$$G^{(2)\nu\nu'\omega}_{kk'q} = \beta G(\vec{k},\nu)G(\vec{k}',\nu')\delta_{\omega 0} - \beta G(\vec{k},\nu)G(\vec{k}'+\vec{q},\nu'+\omega)\delta_{\nu\nu'} \\ - G(\vec{k},\nu)G(\vec{k}+\vec{q},\nu+\omega)F^{\nu\nu'\omega}_{kk'q}G(\vec{k}',\nu')G(\vec{k}'+\vec{q},\nu'+\omega). \quad (2.10)$$

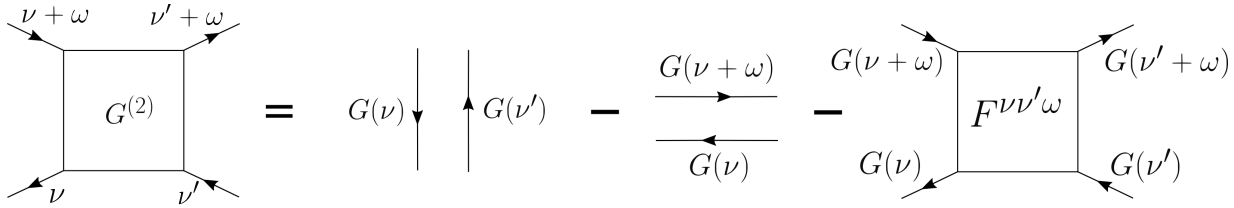

Figure 2.4 – The two-particle Green's function $G^{(2)}$ consists of two disconnected Green's function lines and the connected vertex function F. In this figure, only the frequency arguments have been given for the sake of readability.

Here the so-called particle-hole (ph) notation has been adopted as frequency convention. In ph-notation, $G^{(2)}$ describes the scattering process of an electron and a hole, ω and $\vec{q}$ being the transferred energy and momentum. Another possibility would be to write two-particle quantities in particle-particle (pp) notation, by replacing $\nu+\omega$ with $\omega-\nu'$ and $\nu'+\omega$ with $\omega-\nu$. Then, the two-particle Green's function relates to the scattering of two electrons, where ω and $\vec{q}$ are their total energy and momentum.

The calculation of the two-particle Green's function is important for obtaining physical properties of the system, as it is related to susceptibilities. The generalized susceptibility exhibits full frequency and momentum dependence and reads as

$$\chi^{\nu\nu'\omega}_{kk'q} = -\beta G(\vec{k},\nu)G(\vec{k}+\vec{q},\nu+\omega)\delta_{\nu\nu'}\delta_{\vec{k}\vec{k}'} \\ - G(\vec{k},\nu)G(\vec{k}+\vec{q},\nu+\omega)F^{\nu\nu'\omega}_{kk'q}G(\vec{k}',\nu')G(\vec{k}'+\vec{q},\nu'+\omega), \quad (2.11)$$

therefore differing from $G^{(2)}$ only by substracting the first term.

Susceptibilities describe the linear reaction of the system to an external perturbation within linear response theory [11] and are in general defined for any physical observable A as

$$\chi_A(\tau) = \langle \mathcal{T} A(\tau) A(0) \rangle, \tag{2.12}$$

also known as Kubo formula [12]. When using the charge density operator $n = c^\dagger c$ as observable, one immediately sees when comparing with (2.9), that the corresponding charge susceptibility χ_d associated with density-density correlations is related to the two-particle Green's function.

The physical susceptibility χ_d, which is experimentally accessible, is obtained from the generalized susceptibility by summing over all values of ν,ν',$\vec{k}$ and $\vec{k'}$:

$$\chi_d(\vec{q}, \omega) = \frac{1}{\beta^2 N_k^2} \sum_{\nu\nu'} \sum_{\vec{k}\vec{k'}} \chi^{\nu\nu'\omega}_{kk'q}, \tag{2.13}$$

where N_k is denoting the number of sites in momentum space.

Another interesting quantity is the current-current susceptibility χ_j, using the electrical current operator j, as it is related to the optical conductivity of a system. It is also calculated from the generalized susceptibility evaluated at $\vec{q} = 0$ and given by

$$\chi_j(\omega) = \frac{1}{\beta^2 N_k^2} \sum_{\nu\nu'} \sum_{\vec{k}\vec{k'}} \chi^{\nu\nu'\omega}_{kk'q=0} \frac{\partial \varepsilon_{\boldsymbol{k}}}{\partial k_a} \frac{\partial \varepsilon_{\boldsymbol{k'}}}{\partial k'_a}, \tag{2.14}$$

with $\varepsilon_{\boldsymbol{k}}$ being the dispersion relation of the system and k_a the component of $\vec{k}$ in a certain direction, for example $k_a = k_x$ being the x-component and therefore χ_j refering to the susceptibility of the current in x-direction.

2.2 Parquet equations

We now want to analyze the properties of the two-particle vertex function F appearing in equation (2.10). All diagrammatic contributions to F are one-particle irreducible, which follows directly from particle conservation. To classify diagrams of F, we introduce the concept of *two-particle irreducibility*: A diagram is two-particle irreducible, if it cannot be split into two parts by cutting two Green's function lines G. According to this classification, there are either diagrams that are fully two-particle irreducible, forming the fully irreducible vertex Λ, or diagrams that are two-particle reducible in exactly one of three channels, corresponding to the way the diagram is split into two parts, as illustrated in Fig. 2.5.

These three channels and their corresponding reducible vertices are:

- Particle-hole channel Φ_{ph}: The outer legs 1 and 2 of the diagram can be separated from the outer legs 3 and 4.
- Transversal particle-hole channel $\Phi_{\overline{ph}}$: The legs 2 and 3 can be separated from 1 and 4.
- Particle-particle channel Φ_{pp}: The legs 2 and 4 can be separated from 1 and 3.

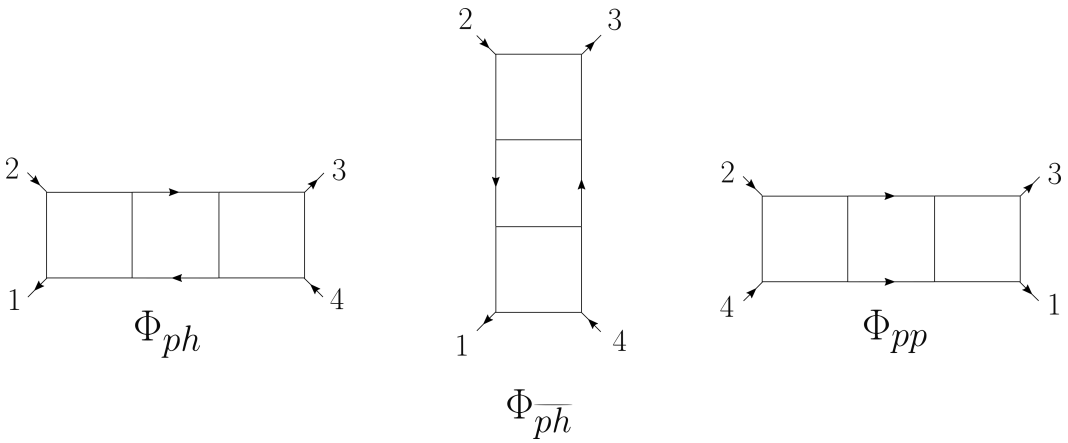

Figure 2.5 – A two-particle reducible diagram can be assigned to exactly one of three channels, according to which two of the four outer legs of the diagram can be separated from the other two. In the particle-hole channel Φ_{ph} legs (1,2) are separated from (3,4), in the transversal particle-hole channel $\Phi_{\overline{ph}}$ (2,3) are separated from (1,4) and in the particle-particle channel Φ_{pp} (2,4) are separated from (1,3). The index of the leg corresponds to the momentum and frequency as $1 \equiv (\vec{k}, \nu)$, $2 \equiv (\vec{k}+\vec{q}, \nu+\omega)$, $3 \equiv (\vec{k}'+\vec{q}, \nu'+\omega)$ and $4 \equiv (\vec{k}', \nu')$.

This classification of F regarding the two-particle irreducibility is summarized in the *parquet equation*

$$F^{\nu\nu'\omega}_{kk'q} = \Lambda^{\nu\nu'\omega}_{kk'q} + \Phi^{\nu\nu'\omega}_{ph,kk'q} + \Phi^{\nu\nu'\omega}_{\overline{ph},kk'q} + \Phi^{\nu\nu'\omega}_{pp,kk'q}. \tag{2.15}$$

To classify the two-particle diagrams further, the vertices Γ_r, being irreducible in one specific channel r, are introduced,

$$\Gamma^{\nu\nu'\omega}_{r,kk'q} = F^{\nu\nu'\omega}_{kk'q} - \Phi^{\nu\nu'\omega}_{r,kk'q}. \tag{2.16}$$

The reducible vertices Φ_r then in turn can be constructed from Γ_r by connecting Γ_r to F by two Green's function lines. These two connecting Green's functions make the diagram reducible in r, as it is done for example for the channel ph in Fig. 2.6. This construction then leads to the so-called *Bethe-Salpeter equations* in all three channels, written in ph-notation as

$$F^{\nu\nu'\omega} = \Gamma_{ph}^{\nu\nu'\omega} + \frac{1}{\beta}\sum_{\nu_1} F^{\nu\nu_1\omega} G(\nu_1+\omega) G(\nu_1) \Gamma_{ph}^{\nu_1\nu'\omega} \tag{2.17}$$

$$= \Gamma_{\overline{ph}}^{\nu\nu'\omega} - \frac{1}{\beta}\sum_{\omega_1} F^{\nu+\omega_1,\nu'+\omega_1,\omega-\omega_1} G(\nu+\omega_1) G(\nu'+\omega_1) \Gamma_{\overline{ph}}^{\nu\nu'\omega_1} \tag{2.18}$$

$$= \Gamma_{pp}^{\nu\nu'\omega} - \frac{1}{2\beta}\sum_{\nu_1} F^{\nu,\nu_1+\omega,\nu'-\nu_1} G(\nu_1+\omega) G(\nu+\nu'-\nu_1) \Gamma_{pp}^{\nu+\nu'-\nu_1,\nu',\omega-\nu'+\nu_1}. \tag{2.19}$$

Here the corresponding momenta arguments have been omitted again for the sake of readability.

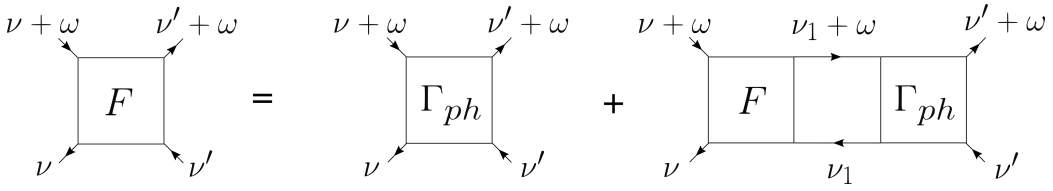

Figure 2.6 – Bethe-Salpeter equation for the ph channel. All diagrams in F can be either irreducible in ph and therefore belong to Γ_{ph}, or reducible in ph, in which case they can in turn be constructed from connecting F with Γ_{ph} by two Green's function lines.

The parquet equation (2.15) together with the three Bethe-Salpeter equations (2.17) – (2.19) make up four equations for the five quantities F, Λ and Φ_r. Often the fully irreducible Λ is assumed to be known and is approximated in different ways, as is done in DΓA and in the DF approach. The simplest possibility is to set it to the bare interaction, i. e. $\Lambda = U$, this is called parquet approximation. As in the Bethe-Salpeter equations also the interacting Green's function G enters, which is connected to the self-energy Σ via the Dyson equation (2.8), we need the Dyson equation and one additional equation in order to find a solution. This equation is the so-called *Schwinger-Dyson equation* or equation of motion, that reads for a purely local interaction U [13]:

$$\Sigma(\vec{k},\nu) = \frac{Un}{2} - \frac{U}{\beta^2}\sum_{\nu'\omega}\sum_{\vec{k}'\vec{q}} F_{kk'q}^{\nu\nu'\omega} G(\vec{k}',\nu') G(\vec{k}'+\vec{q},\nu'+\omega) G(\vec{k}+\vec{q},\nu+\omega). \tag{2.20}$$

The diagram corresponding to this equation is shown in Fig. 2.7.

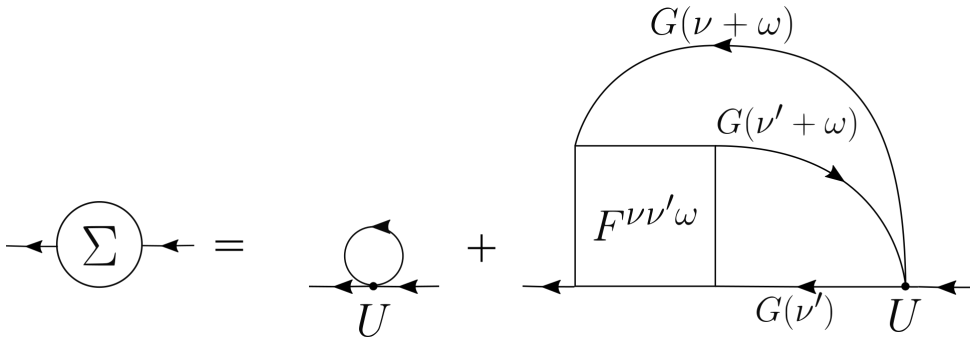

Figure 2.7 – Schwinger-Dyson equation. The first diagram is the Hartree and Fock term and is the contribution of lowest order to the self-energy, while all other one-particle irreducible diagrams with higher order are of the structure as given in the third diagram with the vertex function F.

Solving the parquet equations for a given Λ, hence means to solve the six equations (2.8), (2.20), (2.15) and (2.17) – (2.19) self-consistently, yielding the six quantitites F, Φ_{ph}, $\Phi_{\overline{ph}}$, Φ_{pp}, G and Σ. Note that $\Gamma_r = F - \Phi_r$ can be substituted in the Bethe-Salpeter equations (2.17) – (2.19).

2.3 Dynamical mean-field theory

To calculate the Green's functions of a system, an exact diagrammatic calculation up to infinite order is not possible except for trivial models. For many systems, perturbation theory is applied, in the limit of either weak interactions between electrons or weak hopping of electrons to neighboring sites. However, often most interesting are systems in the intermediate regime, where both kinetic energy and interaction energy are of the same order of magnitude, rendering a perturbative treatment impossible. In this case, a mean-field approach can be applied, as is done in dynamical mean field theory (DMFT) [6, 14]. In DMFT only a single site of a lattice with local interaction is investigated, the rest of the system is treated as a noninteracting bath which hybridizes with the site and therefore generates a time-dependent mean-field coupling to this single site. Electrons can hop to or from the interacting site, but not directly between bath states. This situation corresponds to the solution of an Anderson impurity model (AIM), characterized by a local noninteracting Green's function $\mathcal{G}(\nu)$.

A practical application of DMFT is employed in a self-consistent scheme, described in the following:

1. First from the local noninteracting $\mathcal{G}(\nu)$ of the AIM the local interacting Green's function $G_{\mathrm{loc}}(\nu)$ is calculated. It depends on the investigated lattice model how this step is performed. In the Falicov-Kimball model an analytical expression for $G_{\mathrm{loc}}(\nu)$ exists, which is given in section 2.5.

2. The local interacting Green's function $G_{\mathrm{loc}}(\nu)$ is used to obtain a local self-energy $\Sigma_{\mathrm{loc}}(\nu)$ employing the Dyson equation (2.8) in the form for the AIM:

$$\Sigma_{\mathrm{loc}}(\nu) = \mathcal{G}^{-1}(\nu) - G_{\mathrm{loc}}^{-1}(\nu). \tag{2.21}$$

3. To get back to the full lattice system, the interacting lattice Green's function $G(\vec{k}, \nu)$ is given by the lattice Dyson equation

$$G(\vec{k}, \nu) = \frac{1}{i\nu - \varepsilon_{\boldsymbol{k}} + \mu - \Sigma_{\mathrm{loc}}(\nu)}, \tag{2.22}$$

   where μ is the chemical potential. It can be seen that the local correlations in the lattice enter via the local self energy of the corresponding AIM.

4. The last step is to calculate the local part of the lattice Green's function and compare it to the original G_{loc} from the impurity problem:

$$G_{\mathrm{loc}}(\nu) = \sum_{\vec{k}} G(\vec{k}, \nu). \tag{2.23}$$

   If they are not the same, the calculation is started anew with an updated impurity problem:

$$\mathcal{G}^{-1}(\nu) = \left[\sum_{\vec{k}} G(\vec{k}, \nu) \right]^{-1} + \Sigma_{\mathrm{loc}}(\nu), \tag{2.24}$$

   using again the Dyson equation of the AIM.

The whole DMFT calculation forms a self-consistent cycle, where the four steps listed above are repeated until the condition (2.23) is fulfilled and therefore a convergent result is obtained.

DMFT is a nonperturbative theory, and instead of approximating the number of diagrams taken into account, it approximates the self-energy $\Sigma_{\mathrm{loc}}(\nu)$ to be local and therefore only local correlations are considered. This works quite well for describing physical phenomena dominated by these local correlations, such as the Mott-Hubbard transition, however DMFT fails particularly when describing low dimensional systems or second-order phase transitions, where nonlocal correlations are important. One approach to take such nonlocal correlations into account will be introduced in the next section.

2.4 Dual fermion approach

The dual fermion approach [8] (DF) is a diagrammatic extension of DMFT which aims to take nonlocal correlations into account in addition to the local part of correlations fully treated in DMFT. It is based on the functional integral representation of the Green's function [15] and therefore on the action S, which reads for a model with local interaction U

$$S[c^\dagger, c] = \sum_{i\nu} \left(-i\nu c_i^\dagger c_i + U[c^\dagger, c]\right) + \sum_{\vec{k}\nu} \varepsilon_{\boldsymbol{k}} c_{\vec{k}}^\dagger c_{\vec{k}}, \tag{2.25}$$

where $c_i^\dagger$ and c_i in real space and $c_{\vec{k}}^\dagger$ and $c_{\vec{k}}$ in momentum space are the Grassmann fields corresponding to the creation and annihilation operators. Adding and substracting now a local hybridization function Δ, the action can be split into a local and a nonlocal part:

$$S[c^\dagger, c] = \sum_{i\nu} \left(-i\nu c_i^\dagger c_i + U[c^\dagger, c] + \Delta c_i^\dagger c_i\right) + \sum_{\vec{k}\nu} (\varepsilon_{\boldsymbol{k}} - \Delta) c_{\vec{k}}^\dagger c_{\vec{k}} \tag{2.26}$$

$$= \sum_i S_{\mathrm{loc}}[c^\dagger, c] + \sum_{\vec{k}\nu} (\varepsilon_{\boldsymbol{k}} - \Delta) c_{\vec{k}}^\dagger c_{\vec{k}}. \tag{2.27}$$

The generating functional Z for the Green's function is given as

$$Z[\eta^\dagger, \eta] = \int D[c^\dagger, c] e^{-S[c^\dagger, c] + \sum_{\vec{k}\nu} c_{\vec{k}}^\dagger \eta_{\vec{k}} + \eta_{\vec{k}}^\dagger c_{\vec{k}}}. \tag{2.28}$$

Here the fermionic source fields $\eta^\dagger$ and η have been introduced in Z to obtain the Green's function by the derivation of the generating functional with respect to these source fields and evaluating at $\eta^\dagger = \eta = 0$. To decouple now the local and nonlocal degrees of freedom, a Hubbard-Stratonovich transformation is performed.

The exponential of the nonlocal part of the action then can be written as a Grassmann integral of the new so-called dual fields $\widetilde{c}^\dagger$ and $\widetilde{c}$,

$$e^{-\sum_{\vec{k}\nu}(\varepsilon_{\boldsymbol{k}}-\Delta)c^\dagger_{\vec{k}}c_{\vec{k}}} = \prod_{\vec{k}\nu} b^{-2}(\vec{k},\nu) \int D[\widetilde{c}^\dagger,\widetilde{c}] e^{\sum_{\vec{k}\nu} b^2(\vec{k},\nu)\widetilde{c}^\dagger_{\vec{k}}\widetilde{c}_{\vec{k}} + b(\vec{k},\nu)(\varepsilon_{\boldsymbol{k}}-\Delta)^{1/2}(\widetilde{c}^\dagger_{\vec{k}}c_{\vec{k}} + c^\dagger_{\vec{k}}\widetilde{c}_{\vec{k}})}. \tag{2.29}$$

The generally arbitrary function $b(\vec{k},\nu)$ in this transformation is now chosen for convenience to be

$$b(\vec{k},\nu) = (\varepsilon_{\boldsymbol{k}} - \Delta)^{-1/2} G^{-1}_{\mathrm{loc}}. \tag{2.30}$$

By applying this transformation to the generating functional (2.28), it is possible to integrate out the physical fields by expanding the local part of the generating functional in terms of the coupling between dual and physical fermions, where at order $2n$ the connected n-particle Green's function is obtained. The action for the dual fermions $\widetilde{S}$ is subsequently expressed as

$$\widetilde{S}[\widetilde{c}^\dagger,\widetilde{c}] = -\sum_{\vec{k},\nu} \left[G(\vec{k},\nu) - G_{\mathrm{loc}}(\nu)\right]^{-1} \widetilde{c}^\dagger_{\vec{k}}\widetilde{c}_{\vec{k}} - \sum_i V_{\mathrm{eff}}[\widetilde{c}^\dagger_i,\widetilde{c}_i]. \tag{2.31}$$

The first term in the dual action is quadratic in $\widetilde{c}^\dagger$ and $\widetilde{c}$ and states the free propagator for the dual fermions, $\widetilde{G}_0$, defined as

$$\widetilde{G}_0 = G(\vec{k},\nu) - G_{\mathrm{loc}}(\nu). \tag{2.32}$$

The corresponding dual self-energy $\widetilde{\Sigma}$ is defined via a Dyson equation,

$$\widetilde{\Sigma}(\vec{k},\nu) = \left[\widetilde{G}_0(\vec{k},\nu)\right]^{-1} - \left[\widetilde{G}(\vec{k},\nu)\right]^{-1}. \tag{2.33}$$

The second term of (2.31) depicts the effective interaction V_{eff} between dual fermions, which contains all higher orders in $\widetilde{c}^\dagger$ and $\widetilde{c}$ (fourth, sixth and so on), including the corresponding connected n-particle Green's functions. Regarding the choice of the function $b(\vec{k},\nu)$ to be proportional to the inverse local Green's function, the terms in the effective interaction are appearing without outer legs, and therefore as local n-particle vertex functions. For the FKM, a general analytical expression for these local n-particle vertex functions is given in [16].

As V_{eff} is an infinite sum containing all these n-particle vertex functions, it is however impossible to regard all orders in a numerical approach, and therefore only the first term of V_{eff} is taken into account in practical calculations. In doing so, the effective interaction between dual fermions then is given by the local two-particle vertex F_{loc}:

$$V_{\text{eff}}[\widetilde{c}_i^\dagger, \widetilde{c}_i] = \frac{1}{4} \sum_{\nu\nu'\omega} F_{\text{loc}}^{\nu\nu'\omega} \widetilde{c}_i^\dagger(\nu) \widetilde{c}_i(\nu+\omega) \widetilde{c}_i^\dagger(\nu'+\omega) \widetilde{c}_i(\nu'). \tag{2.34}$$

Noteworthy, in [17] also selected diagrams using the local three-particle vertex have been calculated.

When choosing as Δ the hybridization function of the corresponding impurity from DMFT, the DF approach takes the local Green's function and vertex function resulting from DMFT as diagrammatic building blocks, resulting in the dual fermions being dressed with all local correlations by construction. Then the free dual Green's function (2.32) is completely nonlocal if the self-consistency condition of DMFT is fulfilled.

To obtain the self-energy Σ_{DF} for the real electrons including nonlocal correlations as calculated with the DF approach, the exact relation for mapping the self-energy of the dual fermions to the physical ones is given by

$$\Sigma_{\text{DF}}(\vec{k}, \nu) = \Sigma_{\text{loc}}(\nu) + \frac{\widetilde{\Sigma}(\vec{k}, \nu)}{1 + G_{\text{loc}}(\nu)\widetilde{\Sigma}(\vec{k}, \nu)}. \tag{2.35}$$

Such a mapping makes sure to cancel any one-particle reducible contributions arising in the dual self-energy on the three- or more-particle level. However, when truncating the sum in V_{eff} at the two-particle level, we rather calculate the self-energy for the real fermions by

$$\Sigma_{\text{DF}}(\vec{k}, \nu) = \Sigma_{\text{loc}}(\nu) + \widetilde{\Sigma}(\vec{k}, \nu), \tag{2.36}$$

since no one-particle reducible contributions are included in the first place. A more detailed discussion regarding this matter can be found in [13, 18].

2.5 Falicov-Kimball model

The Falicov-Kimball model (FKM) [5] was introduced in 1969 as a simple model to describe semiconductor-metal transitions. In the FKM, there exist two types of electrons: fully localized ones and mobile ones, which interact with each other via a Coulomb repulsion. The full Hamiltonian for the spinless FKM reads

$$\mathcal{H} = -t \sum_{\langle ij \rangle} c_i^\dagger c_j + U \sum_i c_i^\dagger c_i f_i^\dagger f_i - \mu \sum_i (c_i^\dagger c_i + f_i^\dagger f_i) + \varepsilon_f \sum_i f_i^\dagger f_i, \tag{2.37}$$

where $c_i^\dagger$ and c_i create or annihilate a mobile electron and $f_i^\dagger$ and f_i a localized electron at lattice site i. Contrary to the Hubbard model [4], the hopping t is allowed only for mobile electrons in the FKM, and the local Coulomb interaction U only acts between an itinerant and a localized electron at the same site; μ and ε_f denote the local potentials for c and f electrons respectively. The FKM is the simplest model describing electronic correlations and can also be seen as a simpfliciation to the Hubbard model, when assuming that electrons of one spin species are localized on the lattice sites, while the ones of the other spin species are able to hop between different sites.

In DMFT, a solution of the FKM can be found self-consistently by mapping the problem of the FKM to the corresponding impurity model, the resonant level model (RLM), as described for the general case in section 2.3. The local Green's function for the c electrons is then given by the local noninteracting Green's function $\mathcal{G}$ of the RLM as [19]

$$G_{\mathrm{loc}}(\nu) = p_1 \frac{1}{\mathcal{G}^{-1}(\nu) - U} + p_2 \mathcal{G}(\nu). \tag{2.38}$$

The occupation of the local electrons is indicated by $p_1 = \langle f_i^\dagger f_i \rangle$, and $p_2 = 1 - p_1$. This expression for the local Green's function can be interpreted as a weighted average of two different constellations: In the first term the itinerant electron feels the potential U generated by an immobile electron on the same lattice site, whereas in the second term no f electron is present. From the Green's function, the self-energy Σ_{loc} in DMFT is given by

$$\Sigma_{\mathrm{loc}}(\nu) = \mathcal{G}^{-1}(\nu) - G_{\mathrm{loc}}^{-1}(\nu) = \frac{p_1 U}{1 - p_2 U \mathcal{G}(\nu)}. \tag{2.39}$$

The full lattice Green's function $G(\vec{k}, \nu)$ is then calculated from the self-energy via equation (2.22). In two dimensions, the dispersion relation for the FKM is given by $\varepsilon_{\boldsymbol{k}} = -2t(\cos k_x + \cos k_y)$. Equation (2.23) is then employed to update the local Green's function G_{loc} and close the self-consistent DMFT cycle.

Within DMFT, also the local two-particle vertex function $F_{\mathrm{loc}}(\nu, \nu', \omega)$ can be calculated for the itinerant electrons of the FKM. The mobile electrons can only scatter indirectly via the localized electrons, as the interaction U is just between c and f electrons, which are otherwise noninteracting. This leads to a reduced frequency structure for the local vertex function, only having finite values for $\omega = 0$ and for $\nu = \nu'$. The analytical expression for F_{loc} can be shown [20] to have the following form,

$$F_{\mathrm{loc}}^{\nu\nu'\omega} = \beta(\delta_{\omega,0} - \delta_{\nu,\nu'})a(\nu)a(\nu' + \omega), \tag{2.40}$$

and $a(\nu)$ is given by

$$a(\nu) = \frac{(\Sigma_{\mathrm{loc}}(\nu) - U)\Sigma_{\mathrm{loc}}(\nu)}{\sqrt{p_1 p_2} U}. \tag{2.41}$$

In the two dimensional FKM, a phase transition towards a checkerboard charge density wave (CDW) was proven to occur for a half-filled system [19]. DMFT results including a phase diagram for the 2D FKM can also be seen in [20].

The aim of this thesis is to take nonlocal correlations beyond these DMFT results into account by means of diagrammatic extensions of DMFT. One such approach would be the dynamical vertex approximation (DΓA) [7] which employs the parquet equation based on the local fully irreducible vertex Λ resulting from DMFT to calculate a nonlocal full vertex F. However, DΓA cannot be applied so easily for the FKM, as typically only vertices of c electrons are investigated in DMFT, but to solve the Schwinger-Dyson equation (2.20) mixed f- and c-vertices are necessary. On that account we use the dual fermion approach, introduced in the last section. Previous DF calculations have been restricted to ladder diagrams in a given channel [20, 21]. In this thesis, we employ the more complete parquet equations which are unbiased with respect to a given channel.

3 Parquet dual fermion approach

We now want to employ the DF approach introduced in section 2.4 for the Falicov-Kimball model within a self-consistent parquet formalism using the Bethe-Salpeter equations (BSE) (2.17), (2.18), (2.19) and the parquet equation (PE) (2.15) with the dual Green's functions and vertices. To solve the parquet equation, we apply the parquet approximation, where usually the fully irreducible vertex Λ is approximated by the local interaction U for the real electrons. As the interaction for dual fermions is given by the local vertex function F_{loc}, the fully irreducible dual vertex is approximated here by the corresponding F_{loc} resulting from DMFT, i.e. $\Lambda = F_{\mathrm{loc}}$. In addition to the BSE and the PE, the dual equivalent to the the Schwinger-Dyson equation (2.20) is needed to compute the dual self-energy out of the dual vertex function:

$$\widetilde{\Sigma}(\vec{k},\nu) = -\frac{1}{\beta}\sum_{\nu'}\sum_{\vec{k}'} F_{\mathrm{loc}}^{\nu\nu'\omega=0}\widetilde{G}(\vec{k}',\nu') \\ -\frac{1}{2}\frac{1}{\beta^2}\sum_{\nu'\omega}\sum_{\vec{k}'\vec{q}} F_{\mathrm{loc}}^{\nu\nu'\omega}\widetilde{G}(\vec{k}',\nu')\widetilde{G}(\vec{k}'+\vec{q},\nu'+\omega)\widetilde{G}(\vec{k}+\vec{q},\nu+\omega)\widetilde{F}_{kk'q}^{\nu\nu'\omega}. \quad (3.1)$$

This dual Schwinger-Dyson equation together with the dual Dyson equation (2.33), the BSE and the PE is referred to in the following as *parquet equations*, as they form the set of equations necessary for a self-consistent implementation of the parquet DF approach.

3.1 Implementation

The parquet equations for the DF approach are implemented as shown in Fig. 3.1. The starting point are the results of a DMFT calculation for the FKM, G_{loc}, Σ_{DMFT} and F_{loc}. Using these quantities, the free dual propagator $\widetilde{G}_0$ is calculated according to equation (2.32) and the full dual vertex $\widetilde{F}$ as well as the irreducible vertices $\widetilde{\Gamma}_r$ are initialized to F_{loc}, i.e. $\widetilde{F} = \widetilde{\Gamma}_r = F_{\mathrm{loc}}$. Using these quantities, first the BSE (2.17) – (2.19) are employed to calculate the reducible vertices $\widetilde{\Phi}_r$ in each channel:

$$\widetilde{\Phi}_{ph}^{\nu\nu'\omega} = \frac{1}{\beta}\sum_{\nu_1}\widetilde{F}^{\nu\nu_1\omega}\widetilde{G}(\nu_1+\omega)\widetilde{G}(\nu_1)\widetilde{\Gamma}_{ph}^{\nu_1\nu'\omega} \quad (3.2)$$

$$\widetilde{\Phi}_{\overline{ph}}^{\nu\nu'\omega} = -\frac{1}{\beta}\sum_{\omega_1}\widetilde{F}^{\nu+\omega_1,\nu'+\omega_1,\omega-\omega_1}\widetilde{G}(\nu+\omega_1)\widetilde{G}(\nu'+\omega_1)\widetilde{\Gamma}_{\overline{ph}}^{\nu\nu'\omega_1} \quad (3.3)$$

$$\widetilde{\Phi}_{pp}^{\nu\nu'\omega} = -\frac{1}{2\beta}\sum_{\nu_1}\widetilde{F}^{\nu,\nu_1+\omega,\nu'-\nu_1}\widetilde{G}(\nu_1+\omega)\widetilde{G}(\nu+\nu'-\nu_1)\widetilde{\Gamma}_{pp}^{\nu+\nu'-\nu_1,\nu',\omega-\nu'+\nu_1}. \quad (3.4)$$

Here, again for the sake of readability, only the Matsubara frequency arguments are given, wheras the corresponding momenta arguments have been omitted. The reducible vertices $\widetilde{\Phi}_r$ are further used in the PE (2.15) and in equation (2.16) to obtain the full dual vertex $\widetilde{F}$ and the $\widetilde{\Gamma}_r$ irreducible in each channel:

$$\widetilde{F}^{\nu\nu'\omega}_{kk'q} = F^{\nu\nu'\omega}_{\mathrm{loc}} + \widetilde{\Phi}^{\nu\nu'\omega}_{ph,kk'q} + \widetilde{\Phi}^{\nu\nu'\omega}_{\overline{ph},kk'q} + \widetilde{\Phi}^{\nu\nu'\omega}_{pp,kk'q} \tag{3.5}$$

$$\widetilde{\Gamma}^{\nu\nu'\omega}_{r,kk'q} = \widetilde{F}^{\nu\nu'\omega}_{kk'q} - \widetilde{\Phi}^{\nu\nu'\omega}_{r,kk'q}. \tag{3.6}$$

Subsequently, new $\widetilde{\Phi}_r$ can be calculated out of the updated $\widetilde{F}$ and $\widetilde{\Gamma}_r$ using the BSE (3.2) – (3.4), and out of these again new full and irreducible vertex functions are obtained in the PE (3.5) and (3.6). This first loop of the implementation, including the BSE and PE, is indicated by the yellow box in Fig. 3.1 and each run-through adds new diagrams of higher order in F_{loc} to the dual vertex functions. Hence, the number of iterations in this loop is coined "order" in the following, but keep in mind that the actual order in F_{loc} of the diagrams increases exponentially with each repetition.

Upon concluding the BSE and PE loop, the dual self-energy $\widetilde{\Sigma}$ is calculated from $\widetilde{F}$ and the dual Green's function $\widetilde{G}$ in the dual Schwinger-Dyson equation (3.1). Finally, the dual interacting Green's function is updated via the dual Dyson equation (2.33). This resulting $\widetilde{G}$ then is used as new input quantity in the parquet equations, where now the vertex functions are reset anew at the beginning, i.e. the BSE and PE cycle is started anew beginning from the first order, but with the resulting Green's function from the previous set of repetitions of the BSE and PE loop (up to some order). This second cycle of the parquet approach corresponds to the outer loop denoted in Fig. 3.1. It is depicted by "iteration" in the following, and is repeated until convergence is obtained for the final DF results.

For more details on the specific code used for this algorithm, see appendix A.

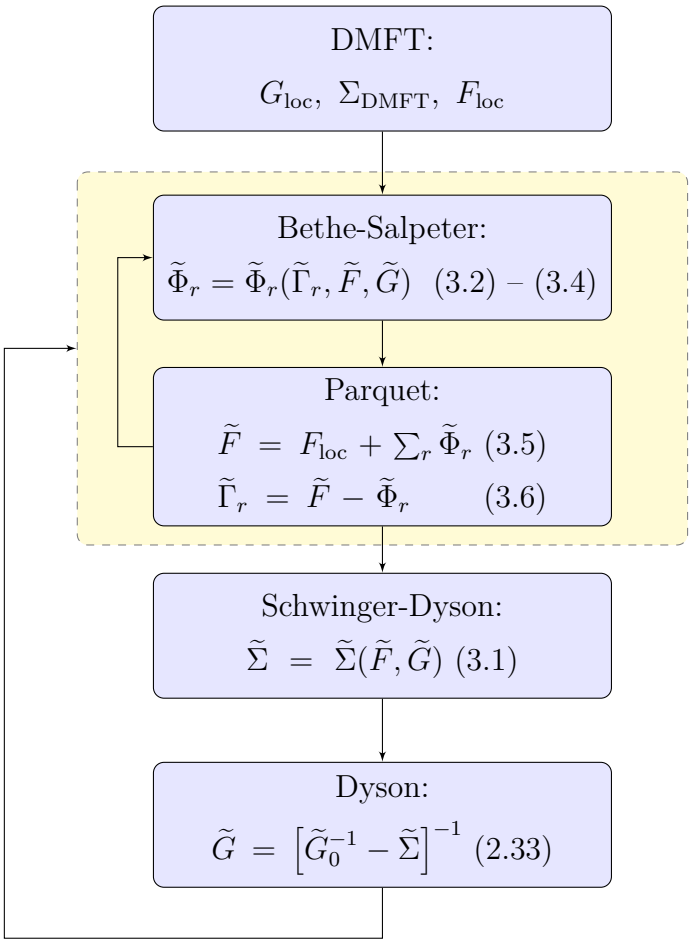

Figure 3.1 – Flow diagram for the parquet dual fermion approach. With the DMFT results G_{loc}, Σ_{DMFT} and F_{loc} as input quantities, the Bethe-Salpeter and in turn the parquet equations are used to build up the dual vertex functions, which is indicated in the yellow box. The number of times these two steps are executed is called "order" in the following and it determines how many diagrams are taken into account for the full dual vertex $\widetilde{F}$. After this Bethe-Salpeter and parquet loop, the dual self-energy is calculated from the dual Schwinger-Dyson equation, followed by the calculation of the dual Green's function via the dual Dyson equation. This resulting $\widetilde{G}$ then is used again as starting point for a new parquet calculation with reset vertex functions beginning from the first order onwards. This second loop is coined "iteration" in the following and the whole calculation is repeated until convergence is obtained for the dual quantities.

3.2 Numerical results

In this section numerical results are presented, calculated by employing the parquet iteration scheme shown in Fig. 3.1. Two differently occupied systems are investigated, indicated by the occupations n_c and n_f of the mobile c and the localized f electrons in the FKM, respectively. These two systems are:

1. A completely half-filled system, $n_c = n_f = 0.5$.

2. A strongly c-doped system where $n_c = 0.15$ while the f band is still held at half-filling, $n_f = 0.5$.

As the calculations within the parquet approach are numerically very cumbersome, only small square lattices with a number of $N_k = 6$ sites in each direction and $N_\nu = 20$ first Matsubara frequencies are considered.

3.2.1 Half-filled system

In the half-filled system, each lattice site has an average occupation of $n_c = n_f = 0.5$ for both types of electrons in the FKM and the chemical potential amounts to half the interaction, $\mu = U/2$. Furthermore, particle-hole symmetry holds at half-filling. Electronic correlations are expected to have maximum effect for this configuration and therefore it is in many cases most interesting to look at the system at half-filling especially when investigating the extension to nonlocal correlations.

In DMFT for the two dimensional FKM at half-filling, a Mott-Hubbard-like metal-to-insulator transition occurs at $U = 1$ [19]. Here and in the following all energies are given in units of $t \equiv 0.25$. The metal-to-insulator-transition can be seen in the DMFT spectral function $A(\omega) = -\frac{1}{\pi}\mathrm{Im}\, G_{\mathrm{loc}}(\omega)$ shown in the left of Fig. 3.2 on the real frequency axis for $U = 0.5$, $U = 0.9$ and $U = 1.5$, where a gap is forming for increasing U and at $U = 1.5$ the spectrum is already split into two subbands.

The parquet DF calculations for the half-filled system have been carried out both at interaction strength $U = 0.5$ and $U = 1.5$. As can be seen in Fig. 3.2, at $U = 0.5$ the system is still metallic, while at $U = 1.5$ it is already insulating. In both cases, convergence for the presented results was ensured by performing five iterations of the parquet scheme, where each iteration was done up to seventh order in the parquet equations. This was verified by looking both at the dual self-energy and the resulting physical susceptibilities. Obtaining such convergent results was directly possible for temperatures from $T = 0.1$ to $T = 0.05$ at

$U = 0.5$ and from $T = 0.1$ to $T = 0.06$ at $U = 1.5$. For lower temperatures, i.e. close to the DMFT phase transition to charge ordering, the calculations become more unstable and obtaining converged results becomes difficult. In principle, the DF transition temperature is lower then the DMFT transition temperature [21], but achieving results in the vicinity of this transition requires a different algorithm where either the order in Fig. 3.1 is increased after each iteration or $\widetilde{F}$ is not reset after each iteration.

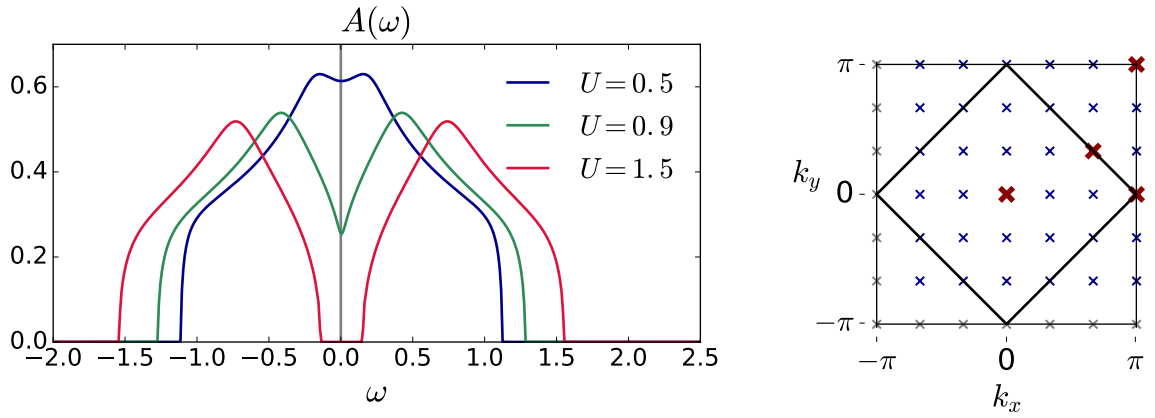

Figure 3.2 – **Left:** DMFT spectral function $A(\omega)$ for the half-filled system, at $U = 0.5$, $U = 0.9$ and $U = 1.5$. At $U = 0.5$ and $U = 0.9$, the system is still metallic. For increasing U, a gap forms and at $U = 1$ the metal-to-insulator transition takes place, as the spectrum is split into two subbands. This can be seen at $U = 1.5$, where the system then is already insulating. **Right:** Brillouin zone with the Fermi surface at half-filling (black line). The 6×6 grid of $\vec{k}$-points for which parquet DF results are presented in this thesis is indicated by dark blue crosses. Note that results for $k_x = -\pi$ or $k_y = -\pi$ are not calculated, as they follow directly from the $\vec{k}$-points on the opposite side of the Brillouin zone due to the symmetry of the FKM. This is why these points are indicated by gray crosses. The red crosses denote the $\vec{k}$-points for which results of the dual self-energy are shown in Fig. 3.3, Fig. 3.4 and Fig. 3.5.

The Fermi surface at half-filling is illustrated in the right of Fig. 3.2, where the $\vec{k}$-points, for which parquet DF results are calculated, are indicated by blue crosses. Results for the dual self-energy in the metallic system at $U = 0.5$ are shown in Fig. 3.3 for $\vec{k} = (\pi, \pi)$, $\vec{k} = (\pi, 0)$, $\vec{k} = (\frac{2\pi}{3}, \frac{\pi}{3})$ and $\vec{k} = (0, 0)$. As can be seen in Fig. 3.2, where these four $\vec{k}$-points are indicated by red crosses, the $(\pi, 0)$- and the $(\frac{2\pi}{3}, \frac{\pi}{3})$-point both lie on the Fermi surface with a, due to particle-hole symmetry, vanishing real part. The (π, π)-point lies outside of the Fermi surface and therefore $\widetilde{\Sigma}$ shows a positive real part there, whereas the $(0, 0)$-point lies inside the Fermi surface with a negative real part of $\widetilde{\Sigma}$. In general, the dual self energy displays a negative imaginary part on the Fermi surface, while the imaginary part is positive

on $\vec{k}$-points away from the Fermi surface, as can be seen in Fig. 3.3. The imaginary part of $\widetilde{\Sigma}$ at $\vec{k} = (\pi, \pi)$ and $\vec{k} = (0, 0)$ is equal. The dual self-energy is shown here for two different temperatures, $T = 0.1$ lying well above the temperature of the DMFT phase transition to charge ordering, and $T = 0.06$ being close to this ordered phase. Correspondingly it can be seen that the amplitude of the dual self-energy is much stronger at lower temperature, which is expected as nonlocal correlations should be enhanced near the transition into a charge ordered phase, where the correlation length increases with decreasing temperature.

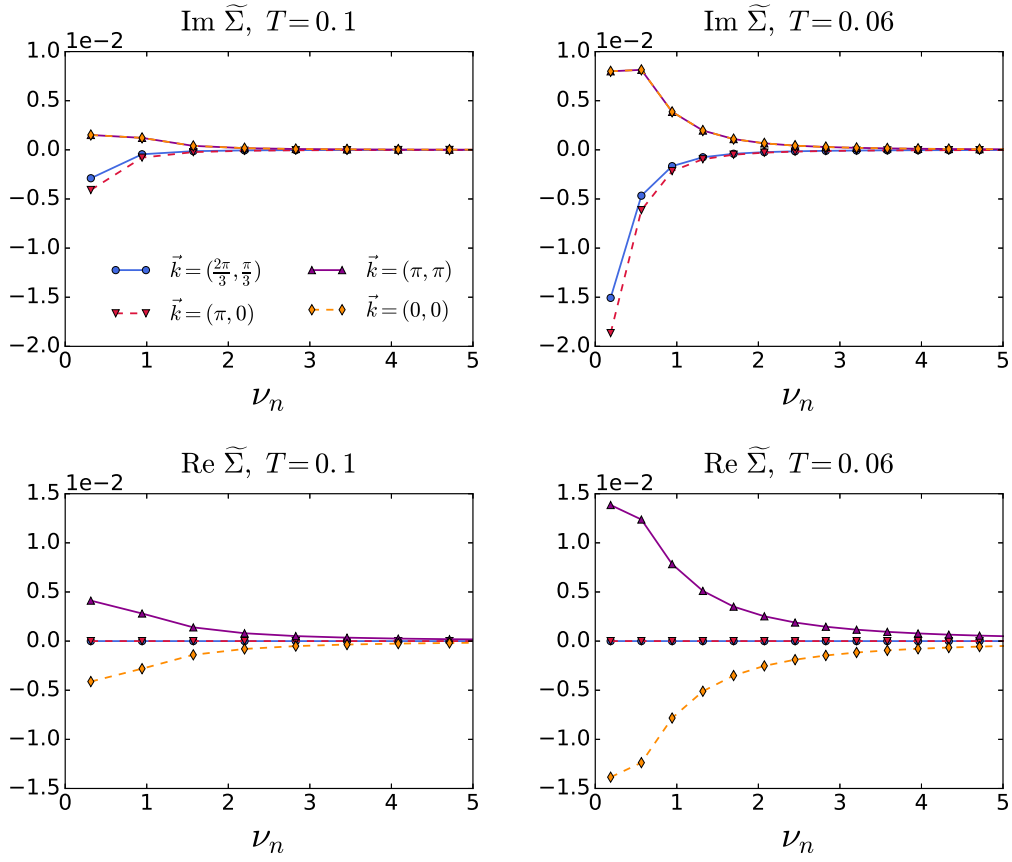

Figure 3.3 – Imaginary part(above) and real part (below) of the dual self-energy at half-filling for the metallic system at $U = 0.5$ at $T = 0.1$ (left) and $T = 0.06$ (right). The self-energy is shown for four points in the Brillouin zone: $\vec{k} = (\pi, \pi)$, $\vec{k} = (\pi, 0)$, $\vec{k} = (\frac{2\pi}{3}, \frac{\pi}{3})$ and $\vec{k} = (0, 0)$. While the $(\pi, 0)$- and the $(\frac{2\pi}{3}, \frac{\pi}{3})$-point lie on the Fermi surface, where the corresponding real part of $\widetilde{\Sigma}$ vanishes, there is a positive real part for the (π, π)-point and negative real part for the $(0, 0)$-point. For the temperature of $T = 0.1$ the dual self-energy is much smaller than the one at $T = 0.06$, affirming that nonlocal correlations play a stronger role at lower temperatures where charge density wave fluctuations become pronounced.

The same results for the dual self-energy, but for the insulating system at $U = 1.5$ are illustrated in Fig. 3.4. Here, the amplitude of the imaginary part of the self-energy is about an order of magnitude larger, and the real part of $\widetilde{\Sigma}$ is even two magnitudes of order larger than at $U = 0.5$. This displays naturally the increasing effect of correlations with greater U. Qualitatively, the DF corrections to the self energy look similar in both cases.

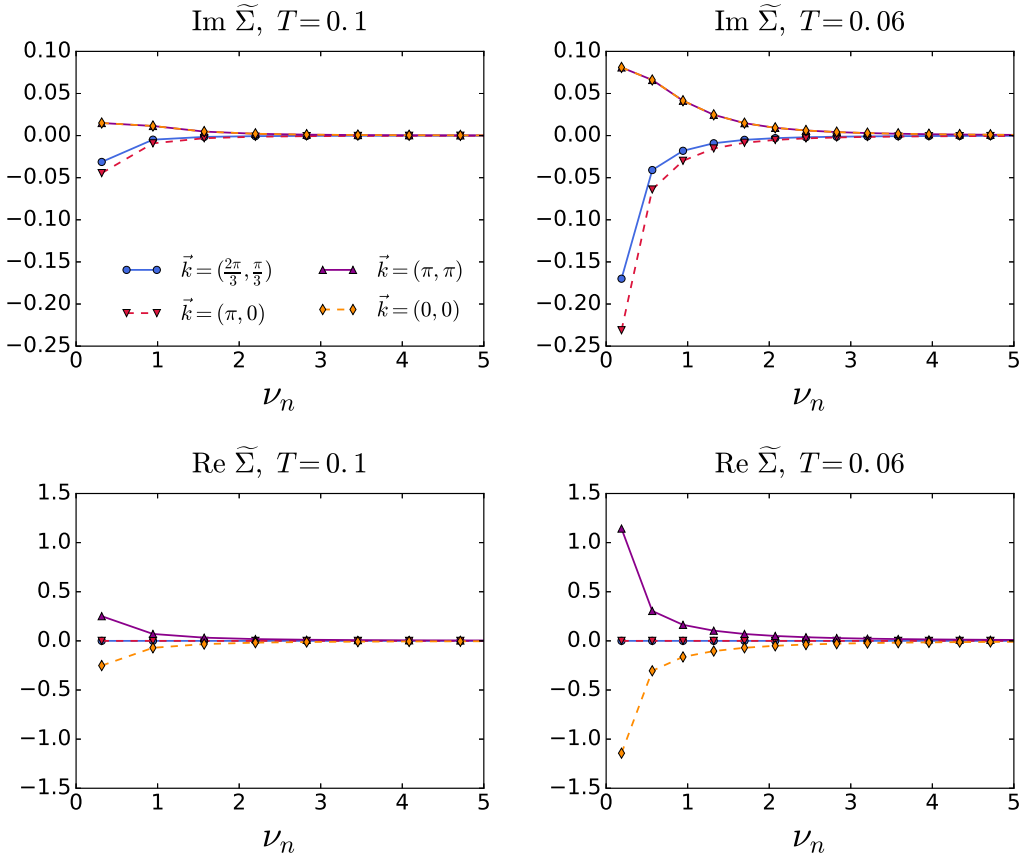

Figure 3.4 – Imaginary part (above) and real part (below) of the dual self-energy at half-filling for the insulating system at $U = 1.5$ at $T = 0.1$ (left) and $T = 0.06$ (right). The self-energy is shown for four points in the Brillouin zone: $\vec{k} = (\pi, \pi)$, $\vec{k} = (\pi, 0)$, $\vec{k} = (\frac{2\pi}{3}, \frac{\pi}{3})$ and $\vec{k} = (0, 0)$. The dual self-energy shows qualitatively the same behavior as for the metallic system in Fig. 3.3, but the imaginary part is one magnitude of order larger and the real part is two magnitudes of order larger then $\widetilde{\Sigma}$ at $U = 0.5$.

From the dual self-energy $\widetilde{\Sigma}$, the lattice self-energy Σ_{DF} of the real electrons is calculated using equation (2.36) and from it the corresponding lattice Green's function G_{DF} results from the Dyson equation (2.22) using the fully $\vec{k}$-dependent self-energy Σ_{DF} instead of the local self-energy from DMFT, Σ_{DMFT}. The imaginary part of these two quantities is shown in Fig. 3.5 compared to the original DMFT results at $T = 0.06$. Σ_{DF} is drawn for the $(\pi, 0)$-point on the Fermi surface, where the dual self-energy is strongest on the lattice, and for the (π, π)-point. The DF self-energy has qualitatively the same behavior as the DMFT self energy but amplifies the effect at $\vec{k} = (\pi, 0)$, wheras it decreases the effect at $\vec{k} = (\pi, \pi)$. Note that for $U = 1.5$ the self-energy is an order of magnitude larger.

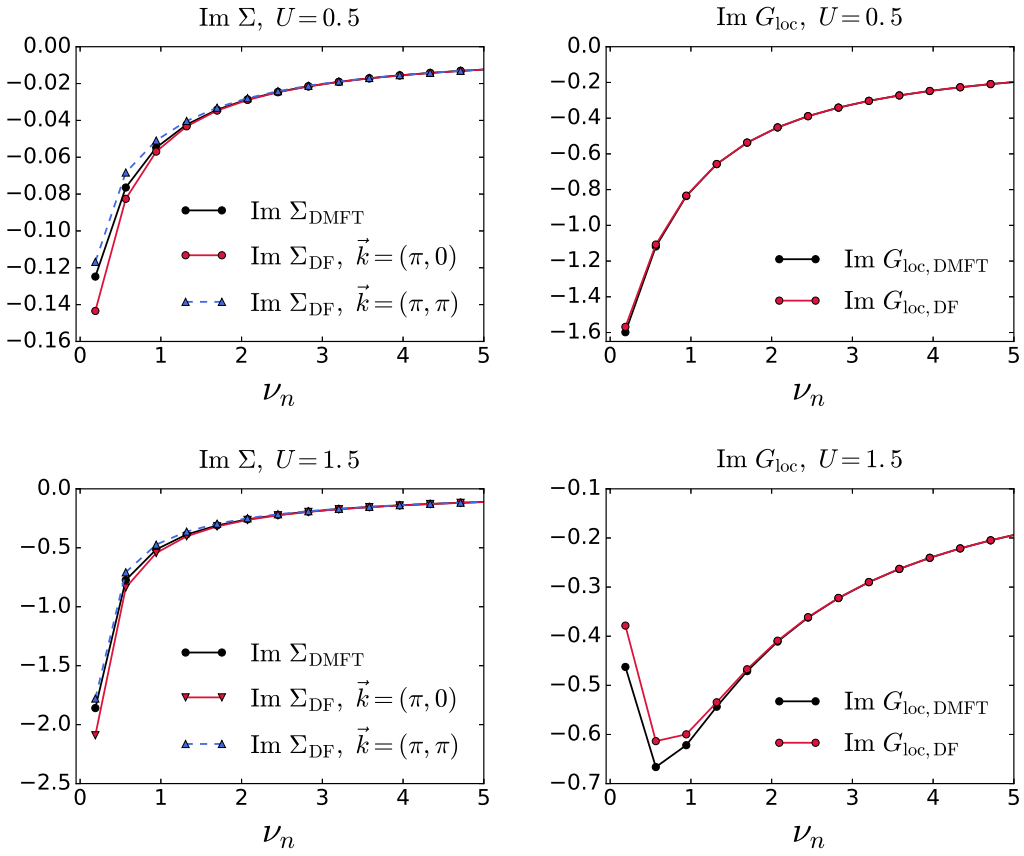

Figure 3.5 – Resulting lattice self-energy Σ_{DF} at $\vec{k} = (\pi, 0)$ and $\vec{k} = (\pi, \pi)$ and local Green's function $G_{\mathrm{loc,DF}}$ compared to the local DMFT results Σ_{DMFT} and $G_{\mathrm{loc,DMFT}}$ at $T = 0.06$ and half-filling for $U = 0.5$ (upper panel) and $U = 1.5$ (lower panel). The increase in the amplitude of the self-energy due to nonlocal correlations leads to a decrease of the local Green's function at small frequencies.

In the right panel of Fig. 3.5, the resulting local Green's function is shown, being the sum of G_{DF} over all 6×6 $\vec{k}$-values. It can be seen that the nonlocal correlations introduced by the DF approach at $U = 0.5$ give only small corrections to the local Green's function for the first few Matsubara frequencies, while at $U = 1.5$ these corrections are considerably larger. As the self-energy is enhanced by the DF extension of DMFT, the Green's function is decreased. Note that a vanishing Im G_{loc} for $\nu_n \to 0$ corresponds to an insulating solution and a finitie value to a metallic one. The DF corrections give rise to a less metallic or more insulating behavior of the system due to nonlocal correlations.

In addition to the self-energy and Green's function, both being one-particle quantities, also the two physical susceptibilites $\chi_d(\vec{q}, \omega)$ and $\chi_j(\omega)$ (in x-direction) are calculated by applying the equations (2.11),(2.13) and (2.14) using the Green's function of the real fermions and the dual vertex function $\widetilde{F}$ obtained in the parquet DF approach as an approximation for the vertex function F of the real electrons. The frequency dependence of $\chi_d(\vec{q}, \omega)$ is illustrated in Fig. 3.6 for $\vec{q} = (\pi, \pi)$, where the amplitude of χ_d is strongest. The susceptibility consists of a disconnected, or "bubble" part, denoted by χ_d^b, and a connected part χ_d^c, based on the full dual vertex $\widetilde{F}$. Both contributions are shown in Fig. 3.6 for two temperatures, both in the metallic case ($U = 0.5$) and the insulating case ($U = 1.5$). The connected part of the static susceptibility at $\omega_n = 0$ strongly increases with decreasing temperature, suggesting the onset of strong charge fluctuations.

It is also interesting to look at the charge susceptibility not only in momentum space, but also in real space, where further aspects of the electronic correlations are visible. This can be seen for the metallic system in Fig. 3.7, where the static susceptibility $\chi_d(\vec{q}, \omega_n = 0)$ on the full lattice at the temperature of $T = 0.06$ is plotted. In momentum space, the value at $\vec{q} = (\pi, \pi)$ is dominating, as it is the $\vec{q}$ - vector that connects the points on opposite sides of the Fermi surface. In real space the charge susceptibility expresses the deviation of the constant occupation of $n_c = 0.5$ at half-filling given that a c electron is found at the origin. Here at $T = 0.06$ the susceptibility shows strong signs of the checkerboard structure expected in the charge ordered phase.

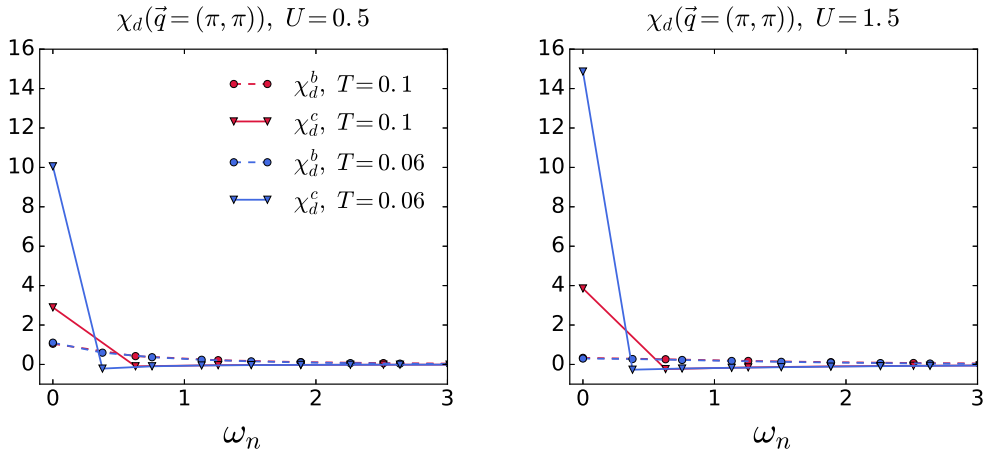

Figure 3.6 – Bubble (χ_d^b) and connected contribution (χ_d^c) to the charge susceptibility χ_d for a half-filled system evaluated at $\vec{q}=(\pi,\pi)$ for the temperatures $T=0.1$ (red) and $T=0.06$ (blue) at $U=0.5$ (left) and $U=1.5$ (right). The connected part of the susceptibility χ_d^c, is much larger than the bubble part χ_d^b and the strong increase at $\omega_n=0$ for lower temperature indicates the vicinity to a phase transition, where the susceptibility would diverge. This behavior is more pronounced at stronger interaction strength U, as here the DMFT phase transition is close to $T=0.06$.

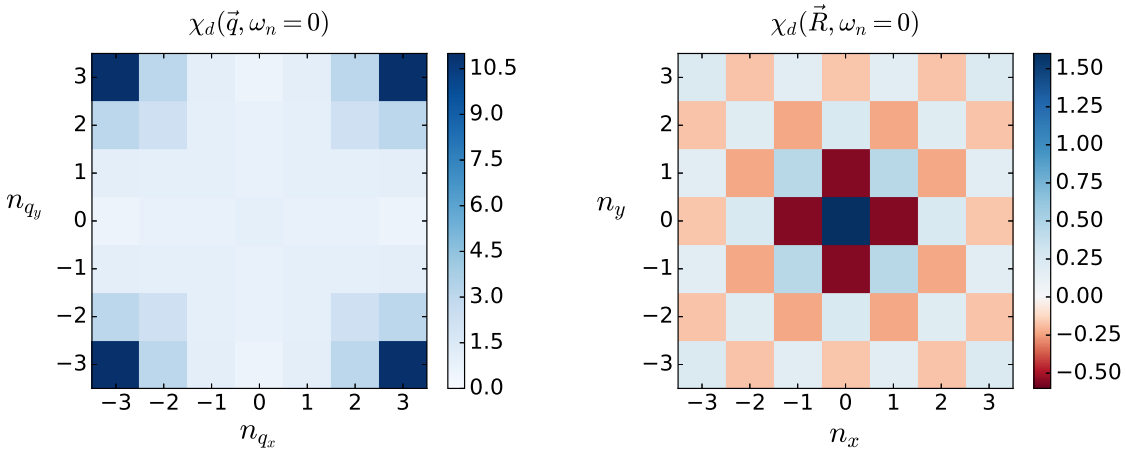

Figure 3.7 – Charge susceptibility χ_d shown in momentum space (left) and real space (right) at $U=0.5$, $\omega_n=0$ and temperature $T=0.06$ for a half-filled system. The indices n_{q_i} and n_i for $i\in\{x,y\}$ specify the corresponding momentum and real space coordinates as $q_i=n_{q_i}\frac{2\pi}{aN_k}$ and $R_i=n_i a$, where the lattice constant is set to $a\equiv 1$. In momentum space, it can be seen that the dominating value lies at $\vec{q}=(\pi,\pi)$, which corresponds to the formation of the checkerboard structure which is also visible in real space.

The susceptibility χ_j denoting the current-current correlation function is shown in Fig. 3.8 for $U = 0.5$ and $U = 1.5$. Again, the two contributions to the full susceptibility, the bubble term χ_j^b and the connected term χ_j^c, are shown separately. In contrast to the charge susceptibility χ_d at half-filling, for χ_j the bubble term is the dominating one. With decreasing temperature the χ_j^c contribution (and therefore the overall susceptibility) increases, as correlations become more significant.

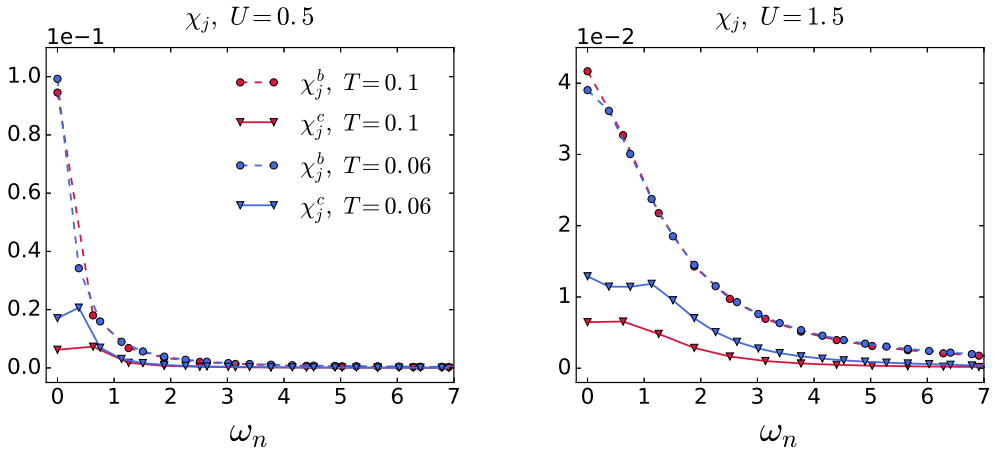

Figure 3.8 – Bubble (χ_j^b) and connected contribution (χ_j^c) to the current-current susceptibility χ_j for the temperatures $T = 0.1$ (red) and $T = 0.06$ (blue) at $U = 0.5$ (left) and $U = 1.5$ (right) for a half-filled system. Overall, the current correlations are much larger in the metallic system at $U = 0.5$ than in the insulating system at $U = 1.5$, which is of course expected. While the bubble term χ_j^b does not change much, the vertex contribution χ_j^c shows an increase with decreasing temperature.

The results of the parquet DF calculation for both physical susceptibilities are compared to the results of DMFT in Fig. 3.9 for the temperature of $T = 0.06$, where the DF corrections are largest. For the one-particle quantities, such as self-energy and one-particle Green's function, the effect of nonlocal correlations is only small (see Fig. 3.5), while for the two-particle quantities, such as the connected contribution to the susceptibility, these nonlocal correlations lead to strong vertex corrections to the DMFT results. This becomes apparent for the static charge susceptibility in the upper panel of Fig. 3.9, where χ_d^{DF}, the susceptiblility calculated in the DF approach, is smaller than the corresponding DMFT susceptibility χ_d^{DMFT} at $\omega_n = 0$. This is expected, as DMFT as a mean field theory generally overestimates the temperature of a phase transition and therefore the divergence in the susceptibility. Regarding the current-current susceptibility, corrections from nonlocal correlations are not so large, as the bubble and not the connected contribution is the leading term of χ_j (Fig. 3.8). The

increase of χ_j^{DF} compared to χ_j^{DMFT} is traced to the connected part, which vanishes in DMFT due to its purely local vertex function F_{loc}, but has positive values in the DF approach.

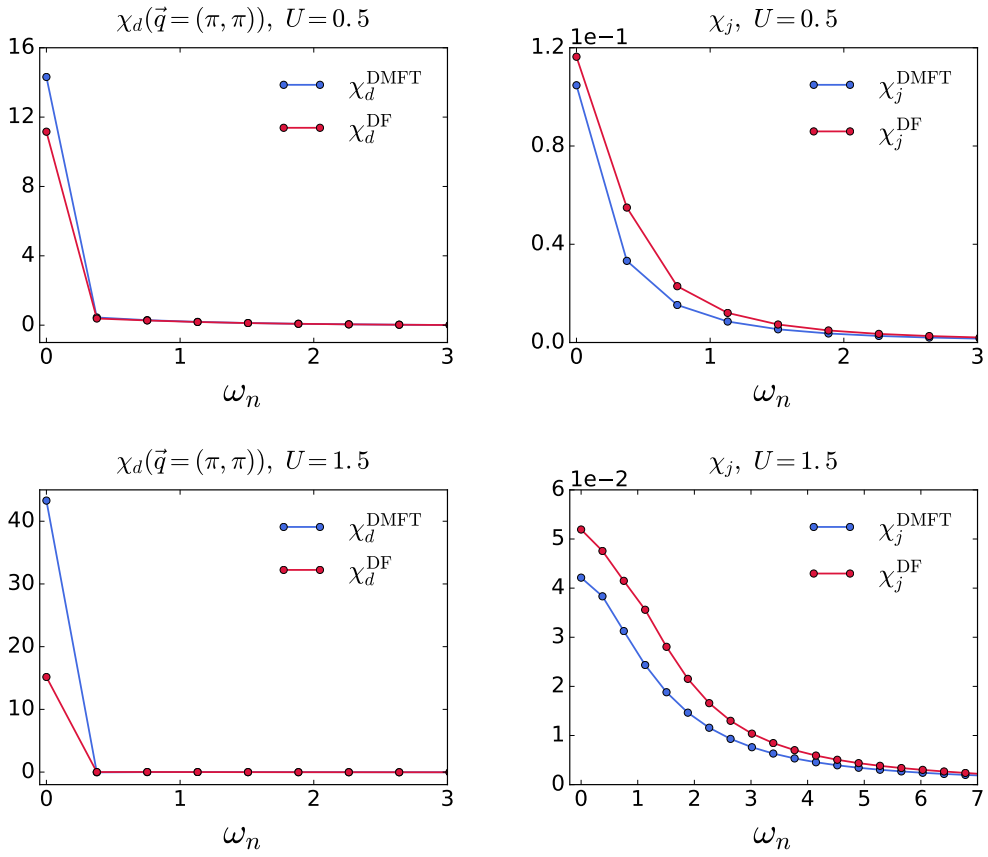

Figure 3.9 – Comparison of the physical susceptibilities for a half-filled system as resulting from parquet DF calculations, χ_d^{DF} (left) and χ_j^{DF} (right), to DMFT results, χ_d^{DMFT} and χ_j^{DMFT}, at $T = 0.06$ for the metallic system at $U = 0.5$ (upper panel), and the insulating system at $U = 1.5$ (lower panel). The nonlocal correlations, taken into account by the DF approach in addition to the local ones in DMFT, show a strong effect for the static charge susceptibility $\chi_d(\vec{q} = (\pi, \pi), \omega_n = 0)$ at this temperature. The increase in χ_j is mainly due to the connected term χ_j^c that is zero in DMFT (because of the purely local vertex F_{loc} in DMFT), but increases for lower temperatures in DF.

3.2.2 c-doped system

In this section, we take a look at the FKM away from half-filling, at least for the c electrons, for which we set the occupation to $n_c = 0.15$, while the occupation of f electrons is still held at $n_f = 0.5$. The deviation from half-filling for the mobile electrons can be given by the sum over all frequencies of the real part of the local Green's function,

$$n_c = \frac{1}{2} + \frac{1}{\beta} \sum_{\nu_n} \mathrm{Re}\ G_{\mathrm{loc}}(\nu_n). \tag{3.7}$$

To fix the number of c electrons, the chemical potential μ, which also depends on temperature, has to be adjusted accordingly. This has been realized in this thesis by finding the corresponding μ to $n_c = 0.15$ for a converged DMFT calculation via a simple bisection method. The resulting chemical potential then was also used for the parquet DF calculation that uses these DMFT results as input. Generally, special care has to be taken here as the corrections on G_{loc} due to DF calculations would change the occupation number compared to DMFT. However, for the following results this fact has been neglected, because the DF corrections are very small and therefore the changes to n_c are only of the order of 1 %.

As the occupation of c electrons is now very low compared to half-filling, no Mott-Hubbard-like metal-to-insulator transition occurs in this configuration and the system retains its metallic character. This can be seen in the DMFT spectral function $A(\omega)$ in Fig. 3.10, shown at $U = 0.5$, $U = 0.9$ and $U = 1.5$. Therefore, only parquet DF results for $U = 0.5$ are presented in this chapter.

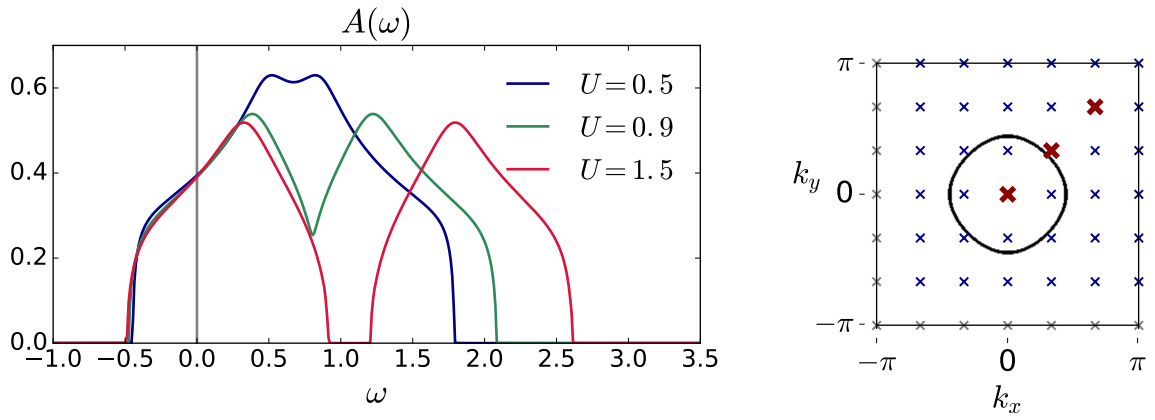

Figure 3.10 – **Left:** DMFT spectral function $A(\omega)$ at filling $n_c = 0.15$ and $n_f = 0.5$. For all three U shown, $U = 0.5$, $U = 0.9$ and $U = 1.5$, the system remains metallic, even when the whole spectrum is split into two subbands at $U = 1$. **Right:** Brillouin zone with the Fermi surface in DMFT for the c-doped system (black line). The DMFT Fermi surface has been determined by the maximum of $A(\vec{k}, \omega = 0)$, actually plotted is simply a region where $A(\vec{k}, \omega = 0)$ is larger than a treshold. The red crosses denote the $\vec{k}$-points for which results of the dual self-energy are shown in Fig. 3.11.

The parquet DF results for the dual self-energy are shown in Fig. 3.11 for $T = 0.1$ and $T = 0.06$, and for three different momenta $\vec{k}$. The $(0, 0)$-point lies of course well within the Fermi surface at the filling of $n_c = 0.15$, $\vec{k} = (\frac{\pi}{3}, \frac{\pi}{3})$ lies very close to it and $\vec{k} = (\frac{2\pi}{3}, \frac{2\pi}{3})$ lies outside of the Fermi surface. The negative offset in the real part of $\widetilde{\Sigma}$ can possibly be traced to the change in the occupation n_c and chemical potential μ in DMFT due to DF corrections, which are enhanced with decreasing temperature. The dual self-energy is altogether much smaller than it is for the half-filled system (Fig. 3.3), which can be expected as nonlocal correlations show the largest effect at half-filling. In the c-doped case, the nonlocal DF corrections are at most about one order of magnitude smaller than the local DMFT self-energy Σ_{loc}, and therefore have negligible effect on the propagator of the real electrons, which is why a comparison of DF and DMFT results for Σ and G_{loc} is not shown here.

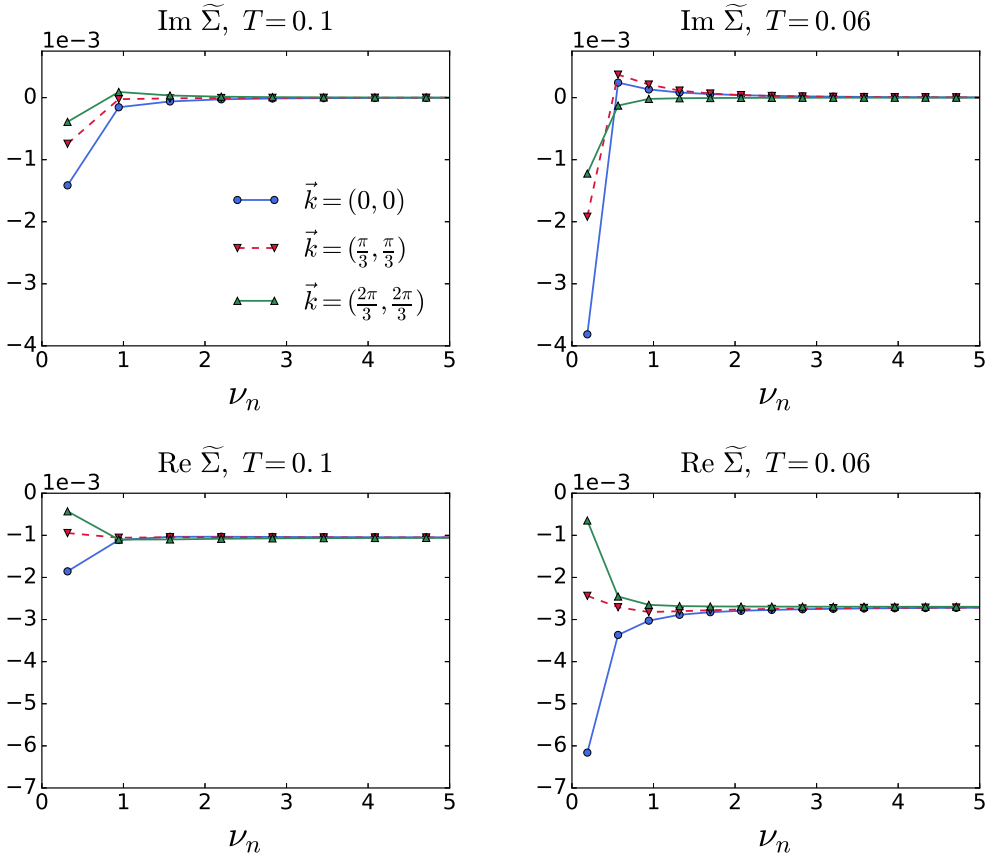

Figure 3.11 – Imaginary part (above) and real part (below) of the dual self-energy at $n_c = 0.15$, $n_f = 0.5$, $U = 0.5$ and for the two temperatures $T = 0.1$ (left) and $T = 0.06$ (right). The self-energy is shown for three points in the Brillouin zone: $\vec{k} = (0,0)$, $\vec{k} = (\frac{\pi}{3},\frac{\pi}{3})$ and $\vec{k} = (\frac{2\pi}{3},\frac{2\pi}{3})$. The dual self-energy is much smaller than for the half-filled system.

The charge susceptibility for the c-doped system is shown in Fig. 3.12 for $\vec{q} = (\frac{\pi}{3}, 0)$, being the point with the strongest value of χ_d here. As the correlations are weaker than in the half-filled system, the static connected contribution $\chi_d^c(\vec{q} = (\pi,\pi), \omega_n = 0)$ is first about half as strong as the bubble contribution at $T = 0.1$, but gets more pronounced at $T = 0.06$. The static susceptibility $\chi_d(\vec{q}, \omega_n = 0)$ and $\chi_d(\vec{R}, \omega_n = 0)$ for the whole lattice in momentum and real space is shown in Fig. 3.13 at $T = 0.06$. The amplitude of χ_d is strongest at $\vec{q} = (\frac{\pi}{3}, 0)$, but not as dominating as it is the case for the (π,π)-point in the half-filled case (Fig. 3.7). This is expected as the Fermi surface for an occupation of only $n_c = 0.15$ lies in the inner region of the Brillouin zone, as can be seen in Fig. 3.10, and hence the corresponding $\vec{q}$-vector connecting opposite sides of the Fermi surface therefore becomes smaller. There is, furthermore, no perfect nesting anymore so that a weaker $\vec{k}$-dependence can be expected

too. In real space, the susceptibility can be interpreted mainly as an on-site correlation of a c electron, as there are on average few electrons ($n_c = 0.15$) on the lattice. Because of this, the value of χ_d is positive for neighboring sites around the origin in contrast to the half-filled case (Fig. 3.7). The system tends to be more localized here, as can be seen from the fast decrease of χ_d in amplitude around the origin compared to half-filling. This is probably due to the fact that the c-doped system at $T = 0.06$ is not in the vicinity of a phase transition as it was the case for the half-filled system at this temperature.

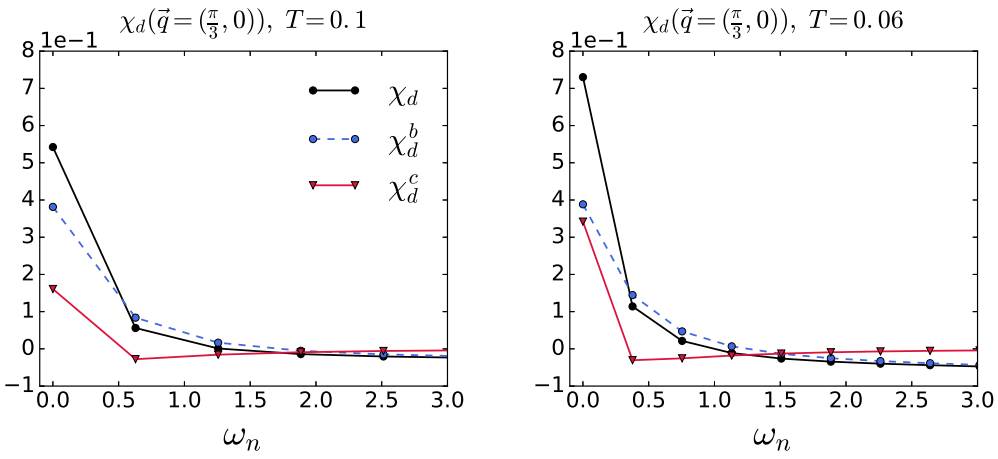

Figure 3.12 – Charge susceptibility χ_d and its bubble (χ_d^b) and connected (χ_d^c) contributions at $\vec{q} = (\frac{\pi}{3}, 0)$ and $T = 0.1$ (left) and $T = 0.06$ (right) for a c-doped system ($n_c = 0.15$, $n_f = 0.5$) at $U = 0.5$. The connected contribution at $\omega_n = 0$ is at $T = 0.1$ smaller than the bubble term, but increases with decreasing temperature.

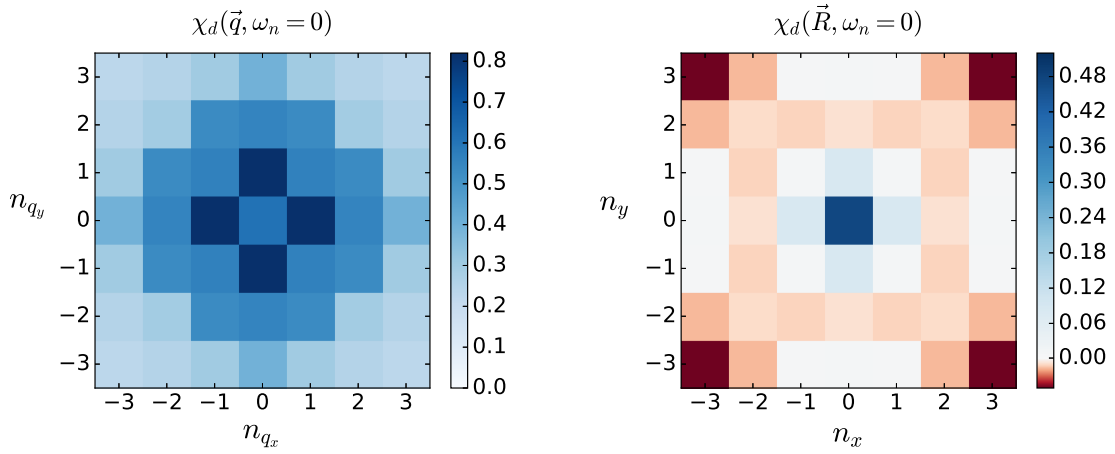

Figure 3.13 – Charge susceptibility χ_d at $\omega_n = 0$, $U = 0.5$ and $T = 0.06$ in momentum space (left) and real space (right) for $n_c = 0.15$, $n_f = 0.5$. The visible features with $\vec{q} = (\frac{\pi}{3}, 0)$ as strongest point are not as distinctive as in the half-filled system (compare Fig. 3.8). In real space, χ_d consists mostly of the on-site correlation of a c-electron and exhibits a tendency towards localization for the electrons, as the amplitude decreases rapidly around the origin.

The current-current susceptibility χ_j is illustrated in Fig. 3.14 for the c-coped system. Again the connected contribution χ_j^c is much smaller than the bubble χ_j^b, but increases with lower temperature. Contrary to the half-filled system, χ_j^c is now negative, resulting in a decrease of the current-current susceptibility and therefore a reduction of the mobility of electrons due to correlations.

When comparing the parquet DF results to the physical susceptibilites of DMFT, as is shown in Fig. 3.15, one sees that the corrections due to nonlocal correlations introduced in the DF approach are much smaller than in the half-filled system (Fig. 3.9), so their effect on χ_d and χ_j is also small. In the case of the charge susceptibility χ_d, the DF results are on top of the DMFT results, and for the current-current susceptibility χ_j it can be seen that the negative vertex corrections lead to a small decrease.

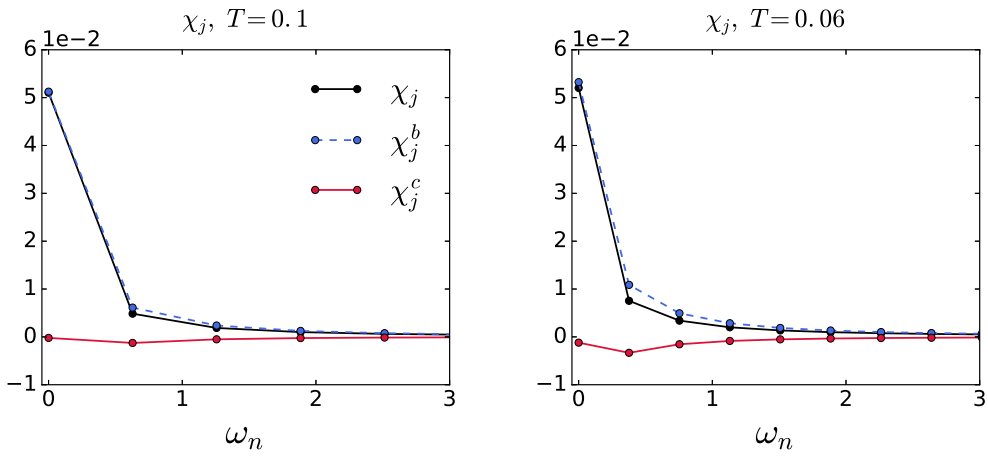

Figure 3.14 – Current-current susceptibility χ_j and its constituting bubble (χ_j^b) and connected (χ_j^c) parts for $T = 0.1$ (left) and $T = 0.06$ (right) in a c-doped system at $U = 0.5$. Note that the connected current-current correlation function χ_j^c has a negative sign, therefore leading to an overall decrease of χ_j.

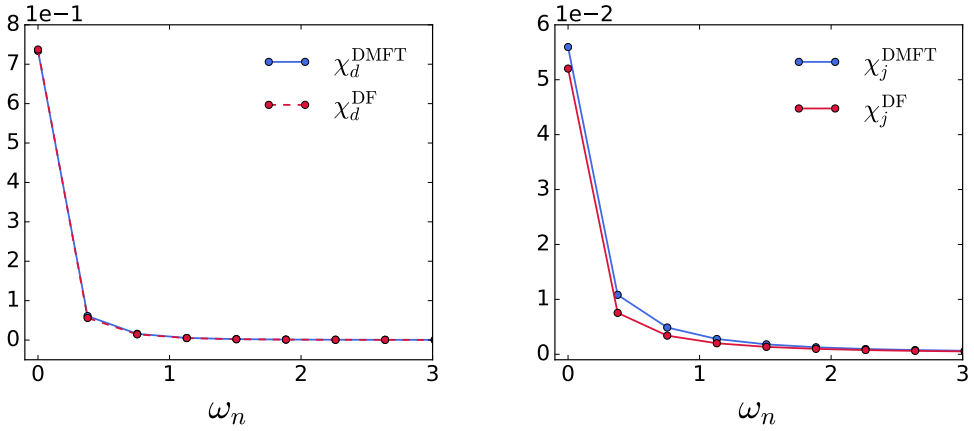

Figure 3.15 – Comparison of physical susceptibilities χ_d and χ_j for a c-doped system with a filling $n_c = 0.15$ and $n_f = 0.5$ of the itinerant and localized electrons, respectively, as calculated in the parquet DF approach and in DMFT, at $T = 0.06$, $U = 0.5$, at the $(\frac{\pi}{3}, 0)$-point in the case of χ_d. There are only minor effects of nonlocal correlations on the susceptibilites for such a doped system.

4 Ladder dual fermion approximation

The full parquet DF calculation introduced in the preceding chapter is numerically very cumbersome, as the full vertex function F depends on three momenta and, in the case of the FKM, two Matsubara frequencies and therefore demands a lot of working memory. This is why only small lattices and frequency ranges are feasible for a parquet implementation, as it is also the case for the numerical results presented up to now, with 6×6 points in the Brillouin zone and 20 frequencies. In an attempt to overcome this huge requirement of computing power, so-called ladder approximations are employed in the DF approach [20–22].

4.1 Implementation

In a ladder approximation for the DF approach, only one channel is considered in the parquet equation (2.15), *ph* or *pp*, instead of all three channels. This is shown diagrammatically in Fig. 4.1 for the full dual vertex $\widetilde{F}$ as built in a *ph*-ladder, where the *ph*-irreducible vertex $\widetilde{\Gamma}_{ph}$ is approximated by F_{loc} (analogous to the full parquet implementation, where the fully irreducible vertex Λ has been approximated by F_{loc}). Note that the vertex of the transversal particle-hole ladder, $\overline{ph}$, can be obtained from the *ph*-vertex using the crossing symmetry:

$$\widetilde{F}^{\nu\nu'\omega}_{\overline{ph},\ kk'q} = -\widetilde{F}^{\nu,\nu+\omega,\nu'-\nu}_{ph,\ k,k+q,k'-k}. \tag{4.1}$$

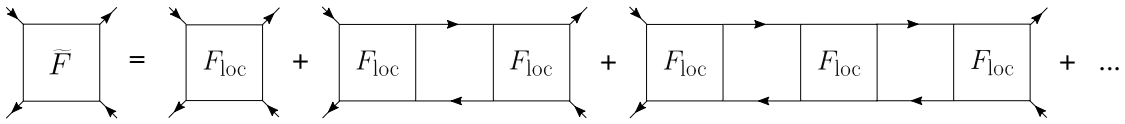

Figure 4.1 – Schematic drawing of the full dual vertex $\widetilde{F}$ built in a *ph*-ladder approximation. The basic building block is in general the *ph*-irreducible $\widetilde{\Gamma}_{ph}$ in such an approach, which has been approximated by F_{loc} in our calculation.

As can be seen easily in Fig. 4.1, the sum for $\widetilde{F}$ corresponds essentially to a geometric series, and therefore $\widetilde{F}$ can be calculated in the ladder DF approximation in principle by an exact analytical expression, schematically written as

$$\widetilde{F} = \frac{F_{\mathrm{loc}}}{1 - \widetilde{\chi}_0 F_{\mathrm{loc}}}. \tag{4.2}$$

Here, $\widetilde{\chi}_0$ denotes the bubble of two dual Green's functions connecting the ladder, calculated in *ph*-notation as

$$\widetilde{\chi}_0(\vec{q},\omega) = \frac{1}{\beta}\sum_{\vec{k},\nu} \widetilde{G}(\vec{k},\nu)\widetilde{G}(\vec{k}+\vec{q},\nu+\omega). \tag{4.3}$$

This shows that a ladder approximation is easily implementable in terms of computational performance and also takes the infinite sum of diagrams into account contrary to the parquet approach, where the calculation has been conducted up to some order. However, within the ladder DF calculation, only a specific class of diagrams is regarded, whereas a convergent parquet calculation can be assumed to approximate the exact solution much better. Furthermore, in the ladder DF approximation different momenta do not couple so that $\widetilde{F}$ only depends on the momentum transfer $\vec{q}$ in the *ph*-channel, or on the total momentum $\vec{q}$in the *pp*-channel. However, one should keep in mind that these ladder diagrams diverge much sooner than the full parquet diagrams when approaching a corresponding phase transition and therefore ladder calculations tend to be less stable than the parquet implementation.

For the ladder DF calculation employed in this thesis, the exact equation (4.2) is not used. Instead, the existing code for the parquet approach has been modified to iteratively build up the ladder diagrams, such as the ones from the *ph*-ladder shown in Fig. 4.1. This was done in order to be able to compare the ladder and corresponding parquet results on an equal footing. The corresponding iteration scheme is illustrated in Fig. 4.2. Analogous to the full parquet DF calculation shown in Fig. 3.1, for the ladder DF calculation the DMFT quantities G_{loc}, Σ_{DMFT} and F_{loc} are used as input and the vertex functions are initialized, $\widetilde{F} = \widetilde{\Gamma}_r = F_{\mathrm{loc}}$. Only one of the BSE is then employed, (3.2) or (3.4), for the *ph*- or the *pp*-ladder to calculate the reducible vertex function $\widetilde{\Phi}_{ph}$ or $\widetilde{\Phi}_{pp}$, respectively. This $\widetilde{\Phi}_r$ then is also the only contribution to $\widetilde{F}$ (apart from F_{loc}) in a version of the PE, i.e. $\widetilde{F} = F_{\mathrm{loc}} + \widetilde{\Phi}_r$. The BSE and the PE using only one channel form a loop that is indicated in the yellow box in Fig. 4.2. The number of times these two equations are performed, coined "order", then determines how many ladder diagrams are taken into account, i.e. after the first use of the BSE and PE the second diagram of the *ph*-ladder in Fig. 4.1, being of second order in F_{loc}, is obtained, and a second run of the loop then adds the third diagram in Fig. 4.1 to $\widetilde{F}$.

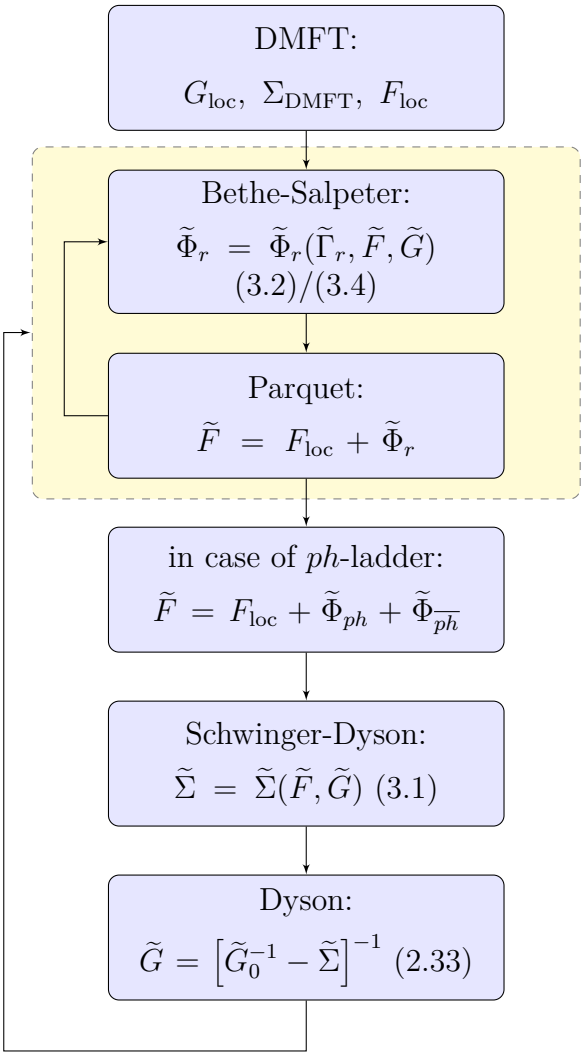

Figure 4.2 – Flow diagram for the ladder dual fermion approximation, with r either $r = ph$ or $r = pp$. Compared to the full parquet calculation shown in Fig. 3.1, here only the reducible vertex $\widetilde{\Phi}_{ph}$ or $\widetilde{\Phi}_{pp}$ is calculated in one of the Bethe-Salpeter equations for the ph- or pp-ladder, respectively. This $\widetilde{\Phi}_r$ is then used as the only contribution to the full dual vertex $\widetilde{F}$ in the parquet equation. The number of times these two steps are executed is again called "order" in the following and it determines how many ladder diagrams are taken into account. After this Bethe-Salpeter and parquet loop, in the case of calculating the ph-ladder, also $\widetilde{\Phi}_{\overline{ph}}$ corresponding to a $\overline{ph}$-ladder is added to $\widetilde{F}$; $\widetilde{\Phi}_{\overline{ph}}$ can be simply obtained by Φ_{ph} via crossing symmetry, i.e. via equation (4.1). Therefore both the ph- and the $\overline{ph}$-ladder contribution enter in the dual Schwinger-Dyson equation when calculating $\widetilde{\Sigma}$. Afterwards, the dual Green's function is updated and then enters the Bethe-Salpeter and parquet loop again. This second loop is coined "iteration" and the whole calculation is repeated until convergence is obtained for the dual quantities.

After the BSE and PE loop, an additional step follows in the case of the ph-ladder. As the reducible vertex $\widetilde{\Phi}_{\overline{ph}}$ in the $\overline{ph}$-ladder can be obtained directly from Φ_{ph} by crossing symmetry using equation (4.1), also these $\overline{ph}$-ladder contributions are added to the full dual vertex, $\widetilde{F} = F_{\mathrm{loc}} + \widetilde{\Phi}_{ph} + \widetilde{\Phi}_{\overline{ph}}$. This vertex function now containing both ph- and $\overline{ph}$-ladder diagrams then enters the dual Schwinger-Dyson equation (3.1). In the case of the pp-ladder however, only $\widetilde{\Phi}_{pp}$ is used for calculating the dual self-energy $\widetilde{\Sigma}$ in (3.1). From $\widetilde{\Sigma}$ the corresponding $\widetilde{G}$ is calculated in the Dyson equation (2.33), which is used as starting point for a new BSE and PE loop to perform a self-consistent calculation of the ladder DF approximation. This corresponds to the second loop in Fig. 4.2 and the number of times this loop is executed is again called "iteration".

4.2 Numerical results

In the following, numerical results for the ladder DF approximation are presented, both for the particle-particle ladder and the particle-hole ladder, where the ladder calculation illustrated in Fig. 4.2 was employed. For the particle-hole ladder, both contributions, ph and $\overline{ph}$, have been taken into account, as described in the last section. The parameters for the results are the same as for the full parquet DF calculation in section 3.2, but for the metallic system at $U = 0.5$ only. To ensure convergent results, five iterations up to seventh order were performed.

4.2.1 Half-filled system

The dual self-energy for a half-filled system calculated in a ph- and a pp-ladder approximation as outlined in Fig. 4.2 is compared to the resulting $\widetilde{\Sigma}$ from the full parquet calculation in Fig. 4.3 for the $(\pi, 0)$-point. Note that we denote the particle-hole ladder by ph here and in the following, but it actually contains both the ph- and the $\overline{ph}$-ladder. For high temperatures, as can be seen in the left panel of Fig. 4.3 for $T = 0.1$, the ph-ladder approach provides almost the same self-energy as the parquet calculation, while $\widetilde{\Sigma}$ as obtained from the pp-ladder is significantly smaller. This indicates a dominance of particle-hole processes for the FKM at half-filling. At low temperatures, as shown for $T = 0.05$, nonlocal correlations become more important and the ph-ladder calculation yields a slightly larger dual self-energy than the parquet calculation.

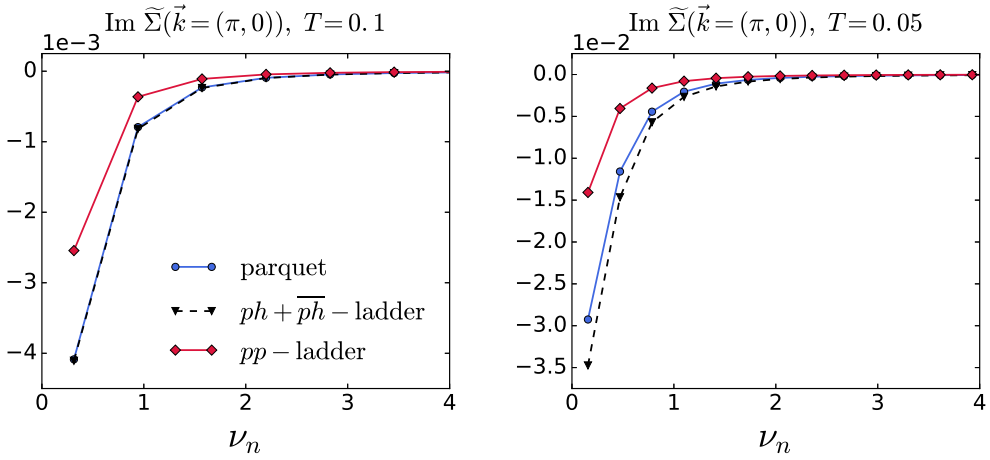

Figure 4.3 – Imaginary part of the dual self-energy at $U = 0.5$, $\vec{k} = (\pi, 0)$ and the two temperatures $T = 0.1$ (left) and $T = 0.05$ (right) for a half-filled system. The results are from three different DF calculations: a full parquet calculation (blue), a *ph*- (black dashed) and a *pp*-ladder (red) approximation. The *ph*-ladder results containing also the $\overline{ph}$-contributions provide a good approximation to the dual self-energy as obtained from the full parquet calculation, at least for high temperatures, while there is a small deviation at lower temperatures.

A similar situation is seen for the charge susceptibility χ_d, for which the three different results (parquet, *ph*- and *pp*-ladder) are shown in Fig. 4.4 for $\vec{q} = (\pi, \pi)$. Only the connected contribution χ_d^c is plotted here, as the bubble term is approximately the same in all three calculations, owing to the actually small DF self-energy corrections of $\widetilde{\Sigma}$. Again, the results from the *ph*-ladder approximation conform well to the ones from the parquet calculation, but with a small deviation at low temperatures (note that the static value at $\omega_n = 0$ is of most interest here as it indicates e.g. phase transitions). The *pp*-ladder approximation however provides a smaller χ_d^c. This shows that it is mainly the *ph*-ladder that contributes to the diverging susceptibility when approaching a phase transition.

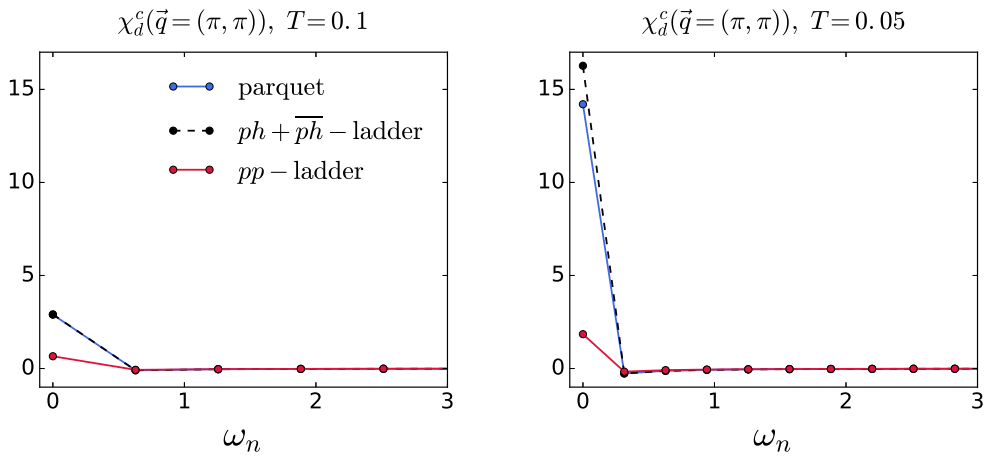

Figure 4.4 – Connected contribution to the charge susceptibility χ_d^c at half-filling and $U = 0.5$ as calculated in the parquet, *ph*- and *pp*-ladder approach. The results are shown at the (π, π)-point and for temperatures $T = 0.1$ (left) and $T = 0.05$ (right). It can be seen that *ph*-reducible diagrams yield the largest contribution to the susceptibility and that they agree with the parquet results at higher temperature, but deviate from the latter with decreasing temperature.

When calculating the connected current-current correlation function χ_j^c, it is important to oberserve that *ph*-ladder contributions with a local F_{loc} as starting point, as shown in Fig. 4.1, vanish. Then the only momentum dependence emerges from the connecting Green's functions, which in turn only depend on the momentum transfer $\vec{q}$. This $\vec{q}$ is zero when calculating the current-current susceptibility, since light only transfers $\vec{q} = 0$ to the electron system. The sum over $\vec{k}$ in equation (2.14) then vanishes, as $G(\vec{k})$ is an even function, while $\frac{\partial \varepsilon_{\boldsymbol{k}}}{\partial k_x}$ is an odd function in $\vec{k}$. The same holds for the sum over $\vec{k}'$. Therefore, only the transversal $\overline{ph}$-ladder diagrams contribute to χ_j^c in our particle-hole-ladder calculation. The results of this $\overline{ph}$-ladder and the *pp*-ladder approximation for the connected contribution to the current-current susceptibility are illustrated in Fig. 4.5. Again, it can be seen that χ_j^c as resulting from the transversal particle-hole ladder approximates the full parquet values well at least at large frequencies, while again results from the *pp*-ladder are very small compared to it. In the next chapter, we will talk in detail about the physical effects bringing about this large contribution in the $\overline{ph}$-channel.

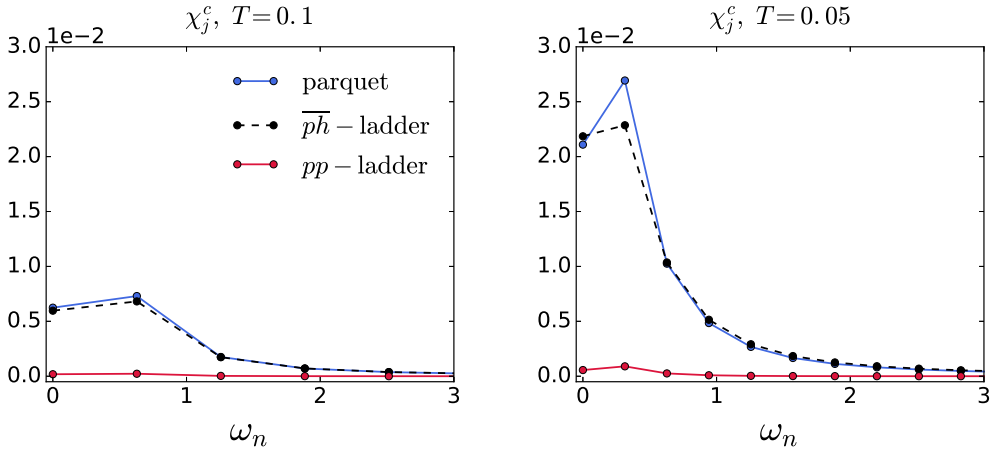

Figure 4.5 – Connected contribution to the current-current susceptibility χ_j^c as calculated in the parquet, *ph*- and *pp*-ladder approach for temperatures $T = 0.1$ (left) and $T = 0.05$ (right) at $U = 0.5$ and half-filling. Note that pure *ph*-reducible contributions vanish. To emphasize this, the corresponding ladder has been denoted by $\overline{ph}$ in the plot, contrary to Fig. 4.3 and 4.4, but the full vertex F used in the calculation is equivalent.

4.2.2 *c*-doped system

We now want to compare ladder and full parquet results also for the *c*-doped system, where $n_c = 0.15$, while the occupation of the f electrons is held at half-filling. The results for the dual self-energy can be seen in Fig. 4.6 at $\vec{k} = (\frac{\pi}{3}, \frac{\pi}{3})$. Results from the *pp*-ladder at $T = 0.1$ now are slightly larger than the corresponding results from the *ph*-ladder or the parquet calculation, at least for this $\vec{k}$-point. At $T = 0.05$ the parquet and *ph*-ladder results (but not the pp ladder) show a qualitatively different frequency behavior than at $T = 0.01$.

Results for the charge susceptibility χ_d^c in the *c*-doped system are shown in Fig. 4.7 at $\vec{q} = (\frac{\pi}{3}, 0)$. They are very similar to the ones in the half-filled case in Fig. 4.4, with the *ph*-ladder results being close to the parquet results, while χ_d^c as calculated in the *pp*-ladder is small. Note that in the *c*-doped system the *ph*-ladder approach yields a lower value than the parquet calculation for the static charge susceptibility $\chi_d^c(\vec{q} = (\frac{\pi}{3}, 0), \omega_n = 0)$, whereas in the half-filled case it yields a larger value.

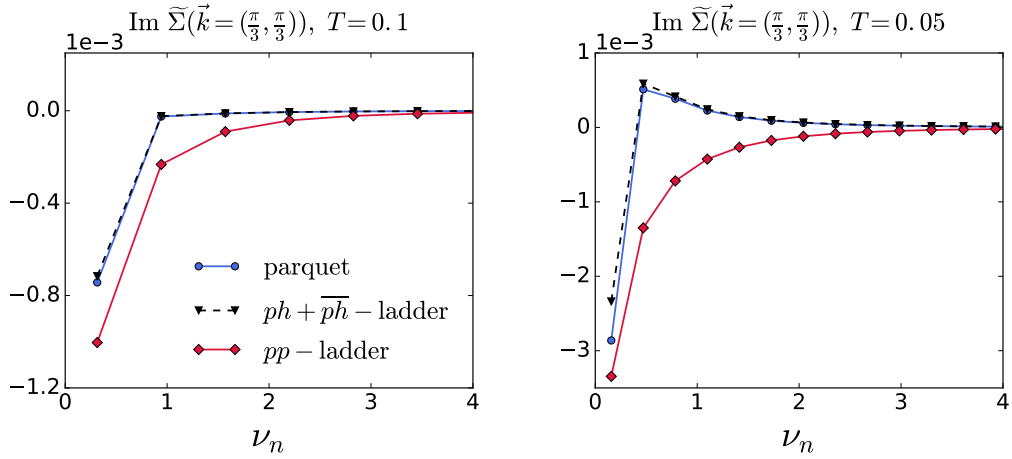

Figure 4.6 – Imaginary part of the dual self-energy at $U = 0.5$, $\vec{k} = (\frac{\pi}{3}, \frac{\pi}{3})$ and the two temperatures $T = 0.1$ (left) and $T = 0.05$ (right) for a c-doped system. The results are from three different calculations: a full parquet approach (blue), a $ph + \overline{ph}$ - (black dashed) and a pp-ladder (red) approximation. As in the half-filled case, the ph-ladder approximates the full parquet results very well, indicating the dominance of the ph-channel in the FKM.

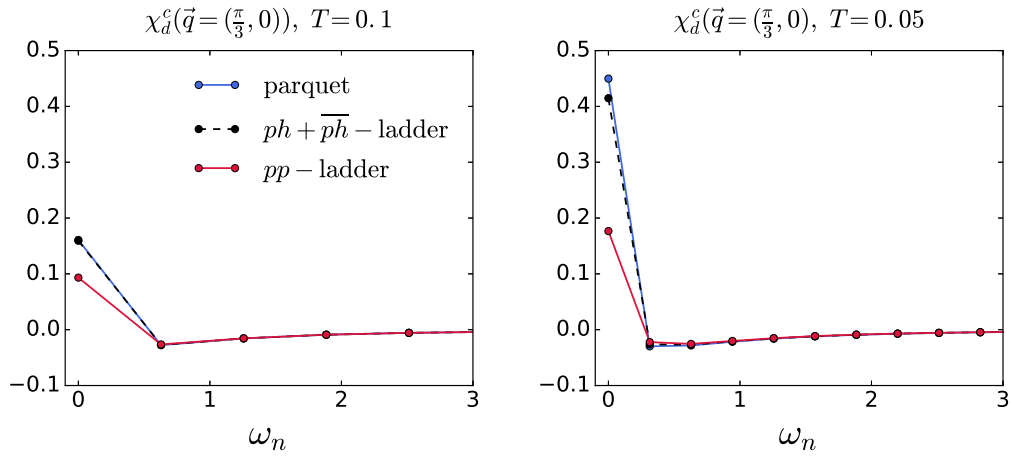

Figure 4.7 – Connected contribution to the charge susceptibility χ_d^c in the c-doped system and at $U = 0.5$ as calculated in the parquet, ph- and pp-ladder approach. The results are shown at the $(\frac{\pi}{3}, 0)$-point and for temperatures $T = 0.1$ (left) and $T = 0.05$ (right). It can be seen that ph-reducible diagrams agree well with the parquet results at higher temperature, but deviate from them with decreasing temperature.

The connected contribution to the current-current susceptibility χ_j^c as calculated by the three different methods is illustrated in Fig. 4.8. We have seen in Fig. 3.14, that χ_j^c resulting from the parquet approach is negative, i.e. has opposite sign as the bubble term χ_j^b. Results from the $\overline{ph}$-ladder (keep in mind that ph-ladder contributions vanish) approximate this result very well, whereas the pp-ladder yields a connected current susceptibility with opposite sign, the same as the bubble term.

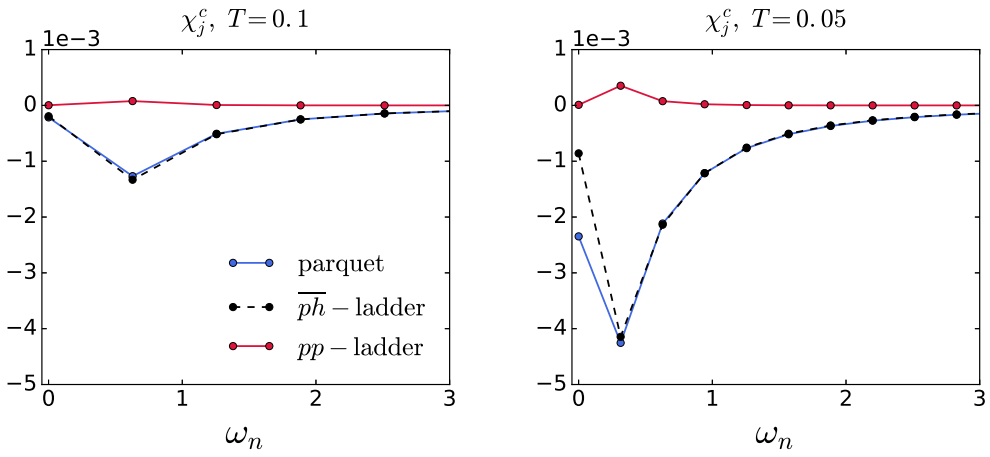

Figure 4.8 – Connected contribution to the current-current susceptibility χ_j^c as calculated in the parquet, ph- and pp-ladder approach for temperatures $T = 0.1$ (left) and $T = 0.05$ (right) at $U = 0.5$ and $n_c = 0.15,\ n_f = 0.5$. Here the pp-ladder results show a positive sign, while the ph-ladder results (with only $\overline{ph}$ nonvanishing) yield a negative sign for the connected term.

5 Optical conductivity

The results presented up till now were calculated on the Matsubara frequency axis ω_n. However, in order to obtain comparable physical quantities, an analytic continuation to the real frequency axis ω is necessary, corresponding to the reversion of the Wick rotation introduced in chapter 2.1. This is formally done for the current-current susceptibility via the continuation $\chi_j(i\omega_n) \to \lim_{\delta\to 0} \chi_j(\omega + i\delta)$. For the numerical data resulting from the parquet DF approach, the analytic continuation is obtained by the maximum entropy method [23,24]. Furthermore, from the current-current susceptibility $\chi_j(\omega)$ on the real frequency axis the optical conductivity $\sigma(\omega)$ is calculated by the relation

$$\sigma(\omega) = \frac{\mathrm{Im}\chi_j(\omega)}{\omega}. \tag{5.1}$$

This equation actually gives only the real part of $\sigma(\omega)$, which is the one we are interested in as the real part corresponds to the absorption of light in the system, which can be measured for actual materials in experiments.

5.1 Optical conductivity in the parquet DF approach

In chapter 3.2.1 the results for χ_j denoting the current-current correlations are presented in Fig. 3.8 for the half-filled system and both before ($U = 0.5$) and after ($U = 1.5$) the metal-to-insulator transition occuring in DMFT for the FKM at $U = 1$. The optical conductivity corresponding to χ_j for these parameters is illustrated in Fig. 5.1. In case of the metal, $U = 0.5$, the bubble conductivity σ^b shows a typical Drude-like peak with maximum conductivity at $\omega = 0$. Including vertex corrections, this value at $\omega = 0$ is strongly reduced, while a peak at around $\omega = 0.4$ is emerging. With lower temperature, the bubble conductivity itself is slightly reduced by the stronger nonlocal corrections in the Green's function, and the effect of the vertex corrections is enhanced. In case of the insulator, i.e. for $U = 1.5$, the bubble conductivity σ^b is centered around $\omega \approx U$, which corresponds to the distance of the peaks of the two subbands in the spectral function shown in Fig. 3.2. Here, the vertex corrections shift the reduced peak to smaller ω. Also there appears to be a nonzero weight of σ at $\omega = 0$ even at $T = 0.06$ due to the effect of the vertex corrections.

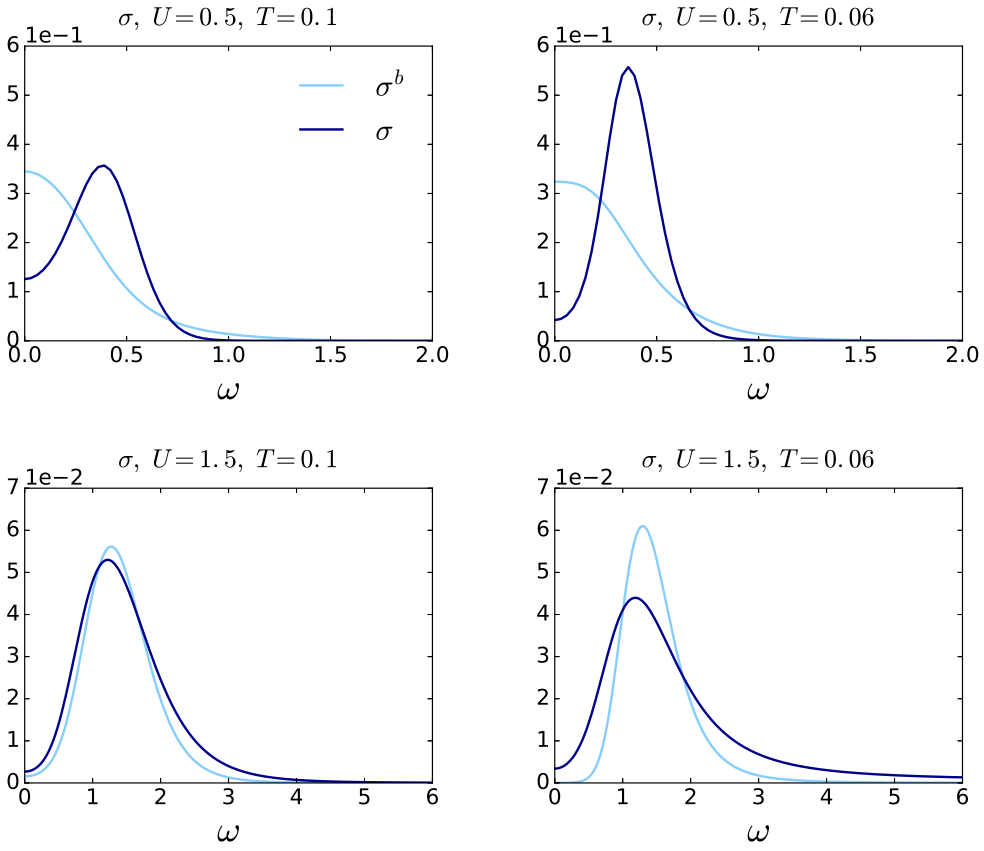

Figure 5.1 – Bubble part σ^b and total optical conductivity σ for the half-filled system at $U = 0.5$ (upper panel) and $U = 1.5$ (lower panel) and at temperatures $T = 0.1$ (left) and $T = 0.06$ (right). At $U = 0.5$, the Drude-like peak of σ^b is transformed to a peak at around $\omega = 0.4$ when including vertex corrections. At $U = 1.5$, the vertex corrections render a smaller peak that is slightly shifted to smaller frequencies. At the lower temperature of $T = 0.06$, the tendencies are similar but the effect of vertex corrections is naturally larger.

It can be seen in Fig. 5.1, that the vertex corrections stemming from the full nonlocal DF vertex function F have a huge effect on the shape of the optical conductivity, and this effect is increasing with lower temperature. To understand where this effect originates from, we take a look at the different contributions to F, classified in the parquet equation (2.15): $F = \Lambda + \Phi_{ph} + \Phi_{\overline{ph}} + \Phi_{pp}$. As the fully irreducible vertex function $\Lambda = F_{\text{loc}}$ in our DF approach, this purely local Λ part does not contribute to the connected part χ_j^c of the current-current susceptibility at all. The nonlocal reducible vertex functions Φ from the ph, $\overline{ph}$ and pp channel however give different contributions to χ_j^c. Note that these contributions are different to a simple ladder calculation in the ph-, $\overline{ph}$- or pp-channel presented in the last chapter, as they additionally contain diagrams that mix such pure ladder diagrams.

These different contributions from the reducible vertex functions are shown in Fig. 5.2 for the same parameters as before. Both in the metallic ($U = 0.5$) and the insulating phase ($U = 1.5$), the clearly dominating contribution to the vertex correction of χ_j is the $\overline{ph}$-channel. Contributions from the *ph*- and *pp*-channel are rather small by contrast. The vertex corrections stemming from the *pp*-channel are a little larger than the ones from the *ph*-channel and show a different behavior for small frequencies. The same situation we have already seen in Fig. 4.5 for the pure $\overline{ph}$-ladder diagrams giving the strongest contribution to χ_j^c.

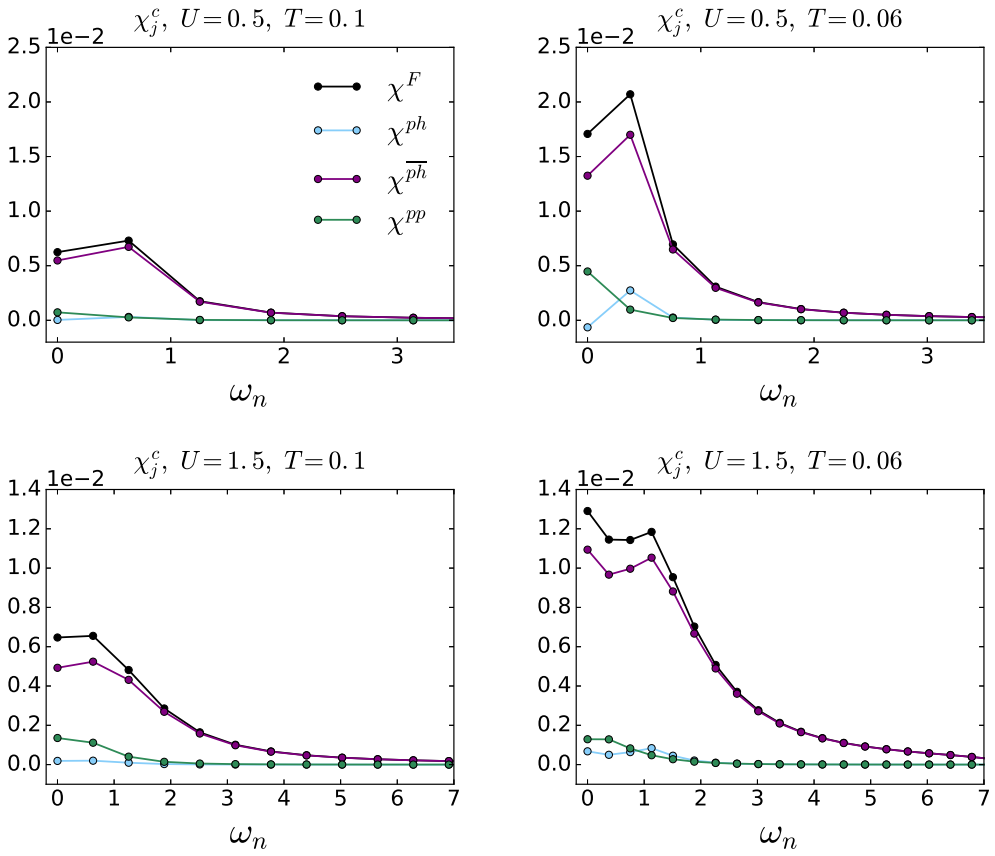

Figure 5.2 – Different contributions to the connected current-current susceptiblity χ_j^c for the same parameters as in Fig. 5.1. The contributions stemming from Φ_{ph}, $\Phi_{\overline{ph}}$ and Φ_{pp} are denoted by χ^{ph}, $\chi^{\overline{ph}}$ and χ^{pp} respectively, while the full vertex correction χ_j^c also shown here for comparison is denoted by χ^F. Apparently the $\overline{ph}$-contribution constitutes the main part of the vertex corrections, whereas χ^{ph} and χ^{pp} are rather small, the *pp*- being a little larger than the *ph*-contribution.

What is the physical process behind the $\overline{ph}$-contribution to the vertex correction of the optical conductivity? The optical conductivity describes the interaction of the solid system with light. A famous example for a bosonic quasiparticle that arises from such an interaction is the exciton [25, 26] appearing in semiconductors. The exciton describes a bound electron-hole pair excited by a photon, as visualized in Fig. 5.3 (a). The corresponding Feynman diagram to the exciton is shown in Fig. 5.3 (b): An incoming photon creates an electron-hole pair that is interacting repeatedly with each other before recombining to a photon again. It can be easily seen that the middle part of this diagram corresponds to a ph-ladder. As the dispersion relation of photons is very steep compared to the electronic bandstructure, there is almost no momentum transfer of the photon to the system, $\vec{q} = 0$.

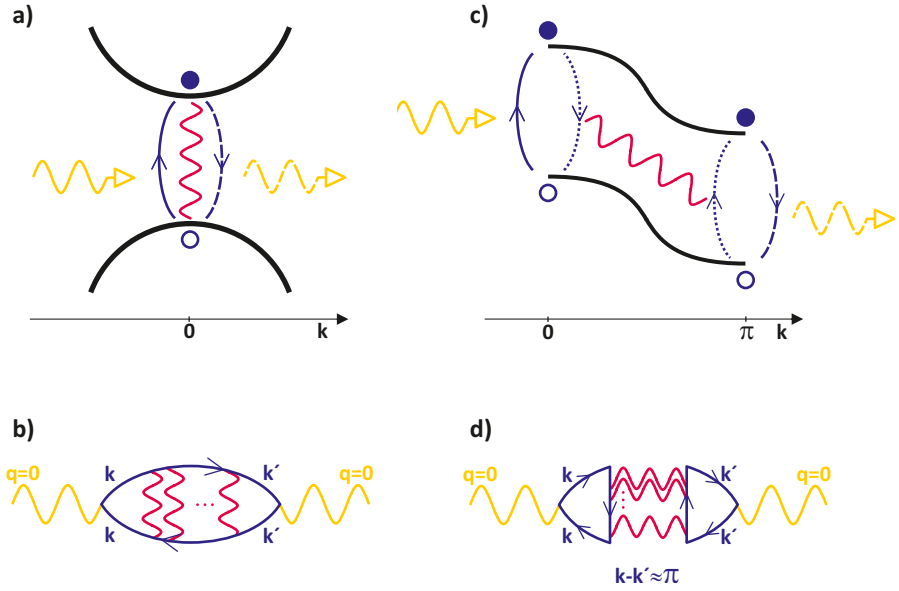

Figure 5.3 – from [9]. Physical processes (top) and corresponding Feynman diagrams (bottom) behind an exciton (left) and the quasiparticles appearing in the half-filled FKM (right). Incoming and outgoing photons are denoted by yellow wiggled lines, an electron-hole pair is symbolized by open and filled circles respectively. Red wiggled lines denote the Coulomb interaction appearing between electron and hole (left) or the two different electron-hole pairs (right).

In the half-filled FKM, a model for strongly correlated systems, charge density wave (CDW) fluctuations are dominating its physics, being especially large near the phase transition to the ordered CDW phase. Such fluctuations are associated with a wave vector $\vec{q} = (\pi, \pi)$, a feature we have already seen in Fig. 3.7 in the density susceptibility $\chi_n(\vec{q})$ being clearly strongest at this point. The Feynman diagrams describing CDW fluctuations correspond

to ph-ladder diagrams as well. We have shown in the last chapter, that it is indeed this ph-channel contribution, and therefore the corresponding fluctuations, that dominate the system. However, the CDW fluctuations with their wave vector at $\vec{q} = (\pi, \pi)$ cannot couple directly to a photon with momentum transfer $\vec{q} = 0$, as in Fig. 5.3 (b). We saw in chapter 4.2.1 that such ladder diagrams even vanish when calculating χ_j^c from a purely local vertex. Instead, the CDW fluctuations couple to light by rotating the ph-ladder 90 degrees, illustrated in Fig. 5.3 (d), resulting diagrammatically in a $\overline{ph}$-ladder with $\vec{k}' - \vec{k} = (\pi, \pi)$. Such a diagram describes a process that is visualized in Fig. 5.3 (c) and is very different to the exciton: An incoming photon creates an electron-hole pair first, and because of the strong Coulomb interaction a second electron-hole pair is created at the wave vector (π, π). The two electron-hole pairs then interact repeatedly with each other before finally recombining to a photon again.

It was shown in [9] that the quasiparticles corresponding to this physical process in Fig. 5.3 (c) originating from $\overline{ph}$-channel contributions appear not only in the FKM (the contribution of this thesis to [9]), but also in other models for strongly correlated systems, such as the Hubbard, the extended Hubbard and the Pariser-Parr-Pople model. As the fluctuations responsible for this phenomena are associated with $\vec{k} = (\pi, \pi)$, in [9] it is proposed to call these quasiparticles π-tons.

To confirm that indeed the (π, π)-contribution is most relevant, the reducible vertex functions $\Phi^{\nu\nu'\omega}_{\overline{ph},kk'q}$ and $\Phi^{\nu\nu'\omega}_{ph,kk'q}$ are illustrated in Fig. 5.4 as a function of $\vec{k}' - \vec{k}$ both for $U = 0.5$ and $U = 1.5$, where $\vec{q} = 0$ for the calculation of the optical conductivity. The ph-contribution Φ_{ph} shows only a weak dependence on $\vec{k}' - \vec{k}$ and is small compared to the contribution $\Phi_{\overline{ph}}$ from the $\overline{ph}$-channel, which is actually peaked at $\vec{k}' - \vec{k} = (\pi, \pi)$ due to CDW fluctuations. It is also due to these fluctuations that the vertex contribution grows when approaching the phase transition at lower temperatures.

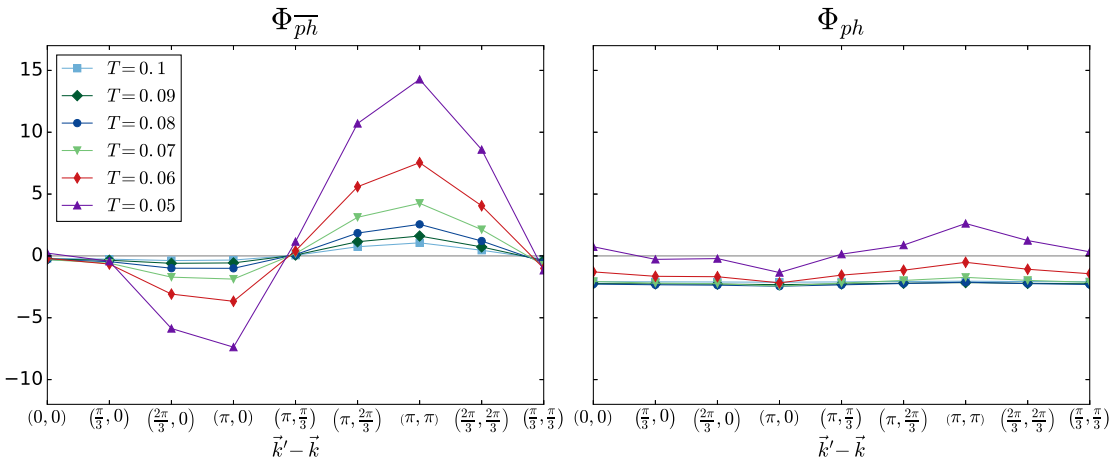

(a) $U = 0.5$

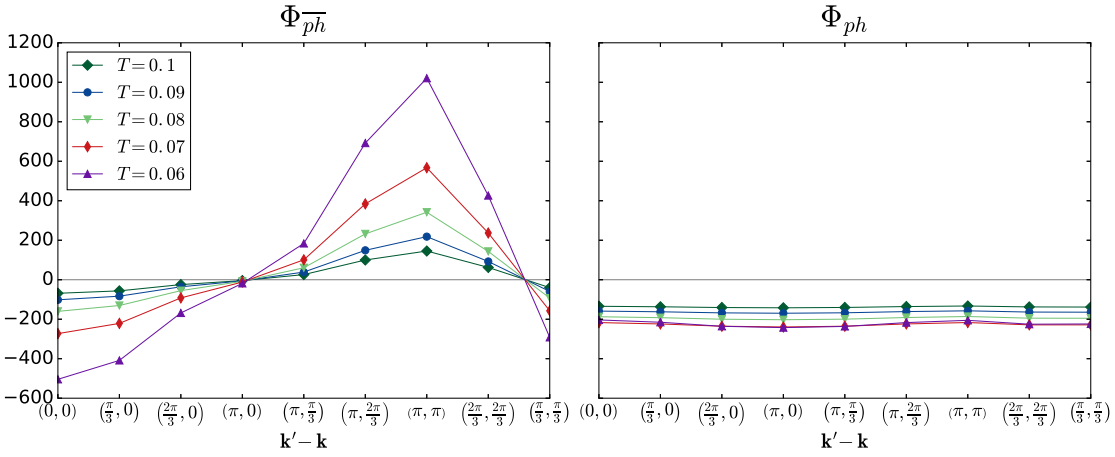

(b) $U = 1.5$

Figure 5.4 – Reducible vertex functions $\Phi_{\overline{ph}}$ and Φ_{ph} at $\nu_n = \nu'_n = \frac{\pi}{\beta}$, $\omega_n = 0$ and $\vec{q} = 0$ as a function of $\vec{k}' - \vec{k}$ with fixed $\vec{k} = 0$. The vertex functions are shown for $U = 0.5$ (upper panel) and $U = 1.5$ (lower panel) for different temperatures. The contribution from the $\overline{ph}$-channel is much larger then the one from the ph-channel and increases with decreasing temperature when approaching the phase transition to the charge ordered phase. The CDW fluctuations responsible for this transition are strongest at $\vec{k}' - \vec{k} = (\pi, \pi)$; $\Phi_{\overline{ph}}$ shows a pronounced peak at this point.

In Fig. 5.5 the results for the optical conductivity also in the c-doped case, $n_c = 0.15$, $n_f = 0.5$, at $U = 0.5$ are shown, corresponding to the results of χ_j in Fig. 3.14. At this c electron occupation, a small second peak is showing in the bubble term σ^b at around $\omega = 1$. This peak corresponds to transitions from the Fermi level to the upper subband in the spectral function shown in Fig. 3.10 and equals the distance from $\omega = 0$ to the location of the peak of the upper subband, which is of course not pronounced much at $U = 0.5$. The small side peak vanishes when including vertex corrections, while optical weight is shifted to $\omega = 0$, resulting in the system to be more metallic. This is contrary to the half-filled case, where the vertex contribution χ_j^c is positive and therefore the optical conductivity is shifted towards larger frequencies by the vertex corrections. In the c-doped system however, these vertex contribution of χ_j are negative.

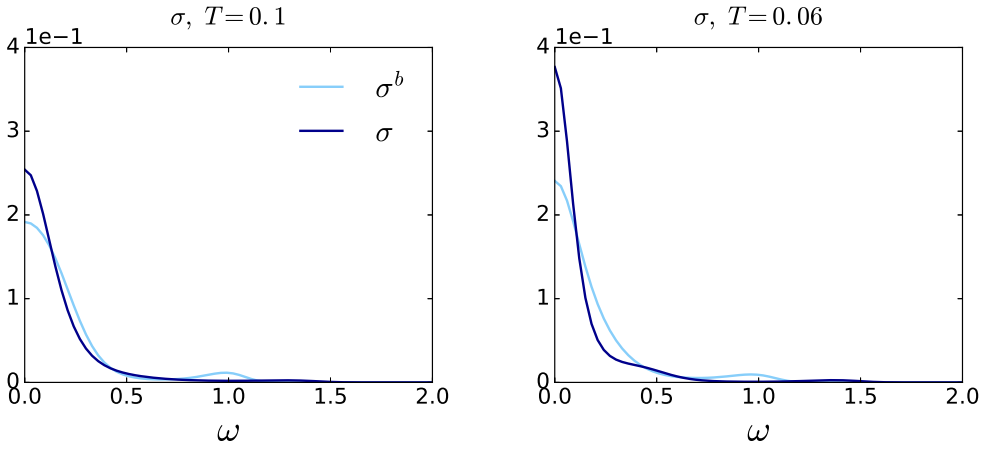

Figure 5.5 – Bubble part σ^b and total optical conductivity σ for the c-doped system, $n_c = 0.15$, $n_f = 0.5$, at $U = 0.5$ and at temperatures $T = 0.1$ (left) and $T = 0.06$ (right). The small peak at around $\omega = 1$ appearing in the bubble vanishes when including vertex corrections, while optical weight is shifted to $\omega = 0$, an effect that increases at lower temperature.

The different contributions to the vertex corrections χ_j^c stemming from the reducible vertices Φ in the respective channels ph, $\overline{ph}$ and pp are illustrated in Fig. 5.6 for the c-doped system. Again the $\overline{ph}$-channel constitutes the largest part of the vertex corrections. The contribution from the pp-channel here shows a different sign than the other two contributions, this was also the case for the pure ladder approximation shown in Fig. 4.8.

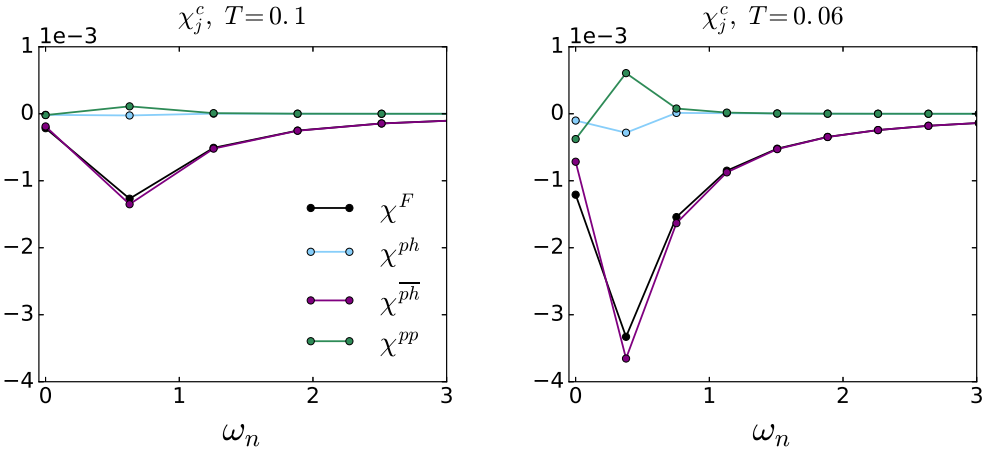

Figure 5.6 – Different contributions to the connected current-current susceptiblity χ_j^c for the same parameters as in Fig. 5.5. Similar to the half-filled case in Fig. 5.2, the $\overline{ph}$-contribution clearly is largest, while the contributions from the *ph*- and the *pp*-channel are rather small. The vertex correction stemming from the *pp*-channel here has a positive sign (except at the first Matsubara frequency), contrary to the other contributions, this was also seen for the *pp*-ladder in Fig. 4.8.

5.2 Optical conductivity in the pp-ladder approach

In the preceding chapter, we took a look at optical excitations originating from the $\overline{ph}$-channel in the parquet equation, the largest vertex corrections to the optical conductivity. Now we want to analyze why we did not observe a different physical phenomenon we expected: weak localization [27]. Weak localization is an effect appearing in disordered electronic systems, such as the FKM, where the conductivity is decreased due to interference terms appearing when averaging over disorder realizations. The Feynman diagrams describing weak localization correspond to *pp*-ladder diagrams, which in a *ph*-presentation correspond to diagrams with maximally crossed interaction lines. Hence, we now study results for the optical conductivity obtained in the *pp*-ladder approach for the FKM.

For the *pp*-ladder results presented before in section 4.2, an adjusted version of the full parquet implementation has been used, as is illustrated in Fig. 4.2. As opposed to this, for the *pp*-ladder results in this chapter, the exact analytical calculation of the dual vertex function $\widetilde{F}$ within the *pp*-ladder approximation is directly employed, i.e. the geometrical series in equation (4.2) is calculated explicitly for the *pp*-ladder:

$$\widetilde{F}_{\vec{q}}^{\nu\nu'\omega} = \frac{F_{\mathrm{loc}}^{\nu\nu'\omega}}{1 - F_{\mathrm{loc}}^{\nu\nu'\omega}\widetilde{\chi}_0(\vec{q},\omega)}. \tag{5.2}$$

Here, $\widetilde{\chi}_0$ is calculated in *pp*-notation,

$$\widetilde{\chi}_0(\vec{q},\omega) = \frac{1}{\beta}\sum_{\vec{k},\nu} \widetilde{G}(\vec{q}-\vec{k},\omega-\nu)\widetilde{G}(\vec{k},\nu). \tag{5.3}$$

The resulting vertex $\widetilde{F}$ then shows a reduced momentum dependence that stems from the connecting Green's function bubble $\widetilde{\chi}_0$, as it only depends on the total momentum $\vec{q}$ (in *pp*-notation). This makes it possible to do calculations on a quite larger 32×32 $\vec{k}$-grid with $N_\nu = 40$ Matsubara frequencies. Whereas in this thesis convergent results for the full parquet calculation are not obtained for temperatures below $T = 0.05$, this is easily feasible now within the *pp*-ladder approximation, as the divergences appearing in the parquet approach hail mainly from the *ph*-channel. The results presented in the following have been calculated without self-consistency, i.e. without calculating the vertex function in a self-consistent way by updating the obtained Green's function, to emphasize the effect of the diagrammatic *pp*-ladder without self-energy corrections and therefore the corresponding relevant excitations.

In Fig. 5.7 results for the optical conductivity $\sigma(\omega)$ at half filling are shown for $U = 0.5$, with the system still being metallic, and at $U = 0.9$, close to the metal-to-insulator transition appearing at $U = 1$. Both only the bare bubble σ^b and the total conductivity σ including vertex corrections are presented. It can be seen that the vertex corrections σ^c yield a negative contribution to the conductivity at small frequencies, an effect that increases with decreasing temperature. This is probably due to weak localization, and it can be seen both for $U = 0.5$, with no gap appearing in the bubble σ^b, and for $U = 0.9$, where the gap in σ arises from the decreased spectral weight at the Fermi energy as precursor to the metal-to-insulator transition.

The same effect is visible in the *c*-doped system, $n_c = 0.15$ and $n_f = 0.5$, in Fig. 5.8. For this filling, there is no metal-to-insulator transition, as the chemical potential lies within the lower band when the spectral function starts to split into two subbands at the metal-to-insulator transition. Therefore, both at $U = 0.5$ and at $U = 0.9$ the bubble conductivity σ^b still shows a Drude-like peak at small frequencies, accompanied by a small side peak corresponding to transitions between the two subbands. At $U = 0.9$, compared to $U = 0.5$, more spectral weight is shifted from $\omega = 0$ to this side peak. Again, vertex corrections clearly lead to a decrease of the bubble term at $\omega = 0$, resulting in the system to be more insulating. We associate such a suppression of the metallic conductivity originating from the *pp*-ladder with weak localization corrections.

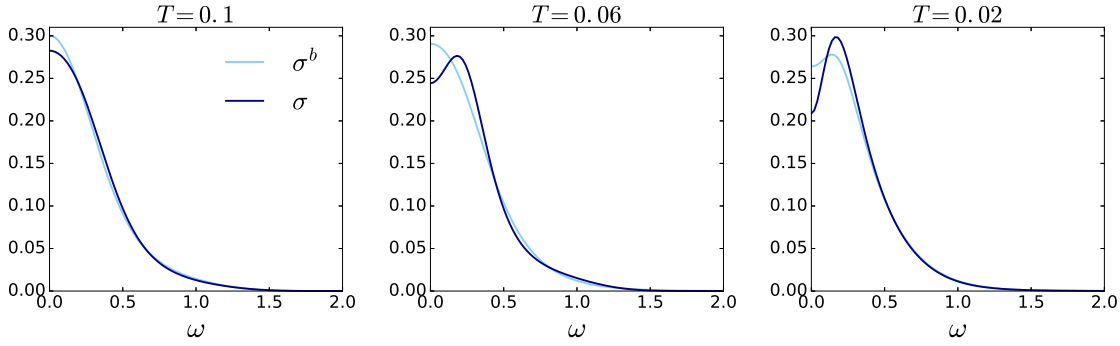

(a) $U = 0.5$

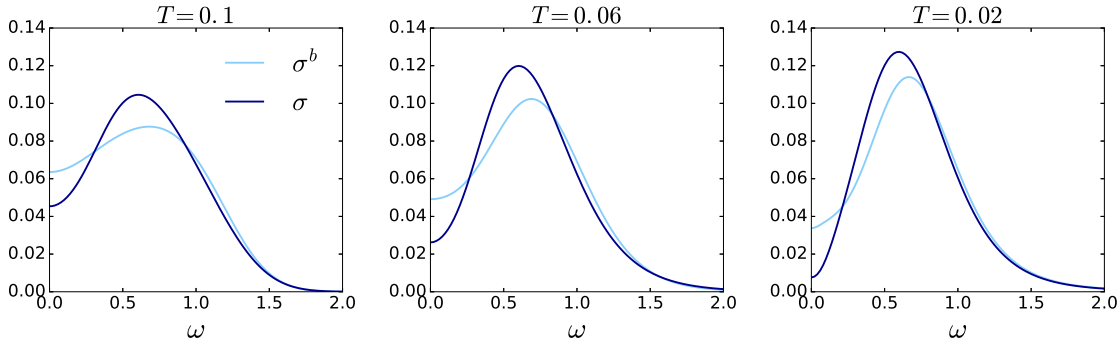

(b) $U = 0.9$

Figure 5.7 – Total optical conductivity σ and bubble term σ^b in the *pp*-ladder approximation without self-consistency at half-filling at the three temperatures $T = 0.1$ (left), $T = 0.06$ (middle) and $T = 0.02$ (right). The results shown in the upper row are at $U = 0.5$, the ones in the lower row at $U = 0.9$. For both U and all temperatures, the *pp* vertex corrections yield a decrease in the optical conductivity at small frequencies. This effect is due to weak localization, and becomes enchanced at lower temperatures.

Hence our conclusion is: There are weak localization corrections if we consider the *pp*-ladder only with a fixed Green's function (fixed interacting self-energy), but these *pp*-contributions are suppressed if we take the *ph*- and $\overline{ph}$-channels into account. Instead of weak localization, π-ton contributions are dominating if we include all channels on an equal footing in the parquet equations.

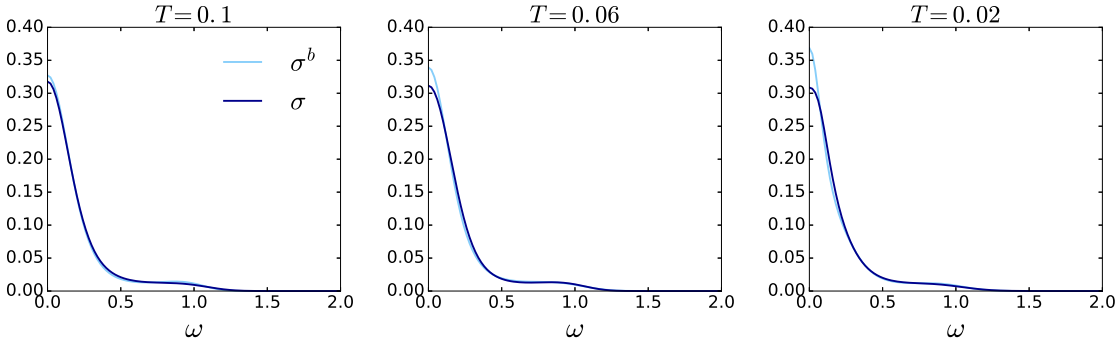

(a) $U = 0.5$

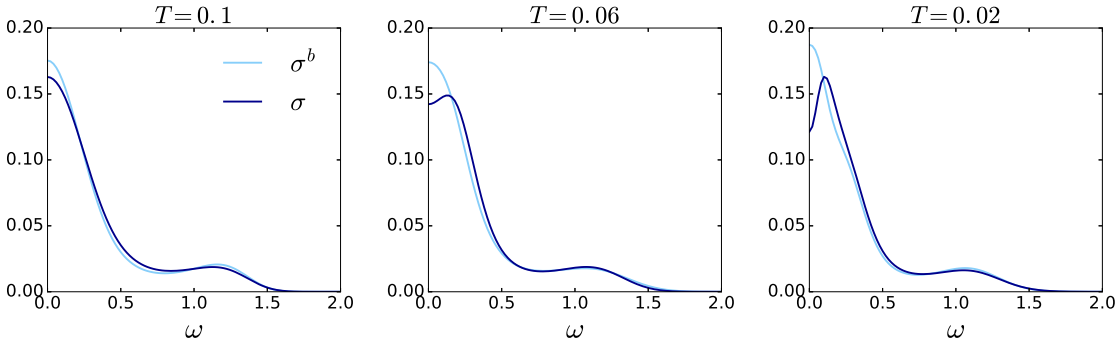

(b) $U = 0.9$

Figure 5.8 – Optical conductivity σ in the *pp*-ladder approximation without self-consistency at doping $n_c = 0.15$, $n_f = 0.5$ and for the three temperatures $T = 0.1$ (left), $T = 0.05$ (middle) and $T = 0.01$ (right). The results shown in the upper row are at $U = 0.5$, the ones in the lower row at $U = 0.9$. Also here in the *c*-doped system the effect of weak localization can be seen, as the weight of the optical conductivity at $\omega = 0$ is reduced due to *pp*-ladder vertex corrections.

6 Conclusion

In this thesis, effects of nonlocal correlations in addition to the local ones as described in DMFT have been analyzed. To this end, a full parquet dual fermion approach was employed to obtain such nonlocal vertex corrections for the Falicov-Kimball model. It is the first time such a full parquet approach is used for this model, giving more information about diagrammatic content than ladder approaches investigated so far [20–22]. This is important to better understand the nature of DF diagrammatics, allowing together with [28] to apprehend phenomena quantitatively and qualitatively.

The resulting nonlocal corrections were found to be largest at half-filling and at low temperatures, as expected. The resulting static charge correlation function χ_d in the DF approach is smaller than in DMFT, showing that the temperature of the phase transition to charge ordering accompanied by the divergence of χ_d is generally overestimated in DMFT.

The parquet results were compared to results obtained by a ladder approximation, using either

(i) both the ladder in the ph- and $\overline{ph}$-channel for calculating the self-energy,

(ii) or the ladder in the pp-channel.

It was confirmed that ph-diagrams corresponding to charge density wave fluctuations are dominating in the FKM, and that such a ladder approach already is a good approximation for the numerically very cumbersome parquet approach. Regarding the current-current correlation function χ_j, it was found that it is the $\overline{ph}$-ladder giving a large contribution contrary to the small contributions from the pp-ladder and the vanishing ones from the ph-ladder results.

The effect of the obtained nonlocal vertex corrections to the optical conductivity was investigated in more detail. When regarding the different reducible contributions Φ_{ph}, $\Phi_{\overline{ph}}$ and Φ_{pp} in the full vertex F for χ_j, the $\overline{ph}$-channel is clearly the dominating one. This is hinting at bosonic optical excitations being prevalent in the FKM that have not been considered hitherto, to the best of our knowledge. The same phenoma was found in other models and is discussed together with the results of this thesis in [9], the corresponding quasiparticles are proposed to be called π-tons.

Finally, it was shown that pp-ladder diagrams lead to weak localization, i.e. a decrease of the optical conductivity with decreasing temperature, though this effect is completely masked by the dominant ph-processes, if these are properly taken into account.

A Description of the parquet dual fermion code

The parquet DF code described in section 3.1 is available on Github [29]. It consists of two different modules that are implemented in C++ and are called in a Python script:

- **SCDMFT**: In this module, a self-consistent DMFT calculation for the FKM is executed, including the calculation of the local vertex function F_{loc} and the free dual propagator $\widetilde{G}_0$ needed as input for the parquet DF calculation.
- **DFParquet**: Here, the full parquet DF approach is implemented, using the quantities calculated in SCDMFT as input. In addition to the dual self-energy $\widetilde{\Sigma}$ and Green's function $\widetilde{G}$, also the physical susceptibilites χ_d and χ_j are calculated and given as output.

The flowchart of the Python code using these two modules is shown in Fig. A.1. First, the necessary input parameters are set, these are listed below with their respective variable names as used in the progam:

beta	inverse temperature β
U	local Coulomb interaction U
mu	chemical potential μ
p1	occupation of f electrons p_1
nkDMFT	number of $\vec{k}$-points for the DMFT lattice
nk	number of $\vec{k}$-points for the DF lattice
nvDMFT	number of Matsubara frequencies for the DMFT calculation
nv	number of Matsubara frequencies for the DF calculation
DMFTiter	number of iterations for the self-consistent DMFT cycle in **SCDMFT**
DFiter	number of iterations for the Bethe-Salpeter and parquet equations in **DFParquet**
iteration	number of times **DFParquet** is called

Usually, the DMFT calculation in **SCDMFT** is done on a much larger $\vec{k}$-grid and with much more Matsubara frequencies than the parquet DF calculation, which is numerically very cumbersome. This is why "nkDMFT" and "nk", as well as "nvDMFT" and "nv" are two different parameters. "DFiter" sets the number of times the Bethe-Salpeter and parquet equations are called in **DFParquet**. This loop was coined "order" before and is indicated in the yellow box of Fig. 3.1, where the general flow diagram of the parquet DF algorithm is shown. By "iteration", the number of times the module **DFParquet** is called is fixed, corresponding to the number of times the dual self-energy and Green's function are updated

after a run-through of the Bethe-Salepter and parquet equations. This was also coined "iteration" before and corresponds to the outer loop in Fig. 3.1.

After setting the parameters, the corrections for the DMFT self-energy Σ_{corr} are initialized to zero. This quantity can be used in an implementation with outer self-consistency, where the self-energy corrections of a previous DF calculation are taken into account as new starting point for the DMFT calculation. This was not the case in this thesis.

Then, the module **SCDMFT** is called. It reads a possible Σ_{corr} and the parameters as input and gives the local self-energy Σ_{DMFT}, local Green's function G_{loc}, local vertex function F_{loc} and the purely nonlocal free dual Green's function $\widetilde{G}_0$ as output.

Before calling **DFParquet** the first time, the dual self-energy $\widetilde{\Sigma}$ is set to zero. The module **DFParquet** reads in this $\widetilde{\Sigma}$, the parameters and the quantities F_{loc}, G_{loc} and $\widetilde{G}_0$ calculated in **SCDMFT** and executes essentially the parquet DF algorithm that is shown in Fig. 3.1 except for the outermost loop there. The quantities that are calculated and given as output are $\widetilde{\Sigma}$, $\widetilde{G}$ and separately the bubble and connected contributions to the physical susceptibilites χ_j and χ_d. The output data is copied and saved to some specific directory by the Python program, before **DFParquet** is started anew, now with the resulting $\widetilde{\Sigma}$ from the previous run-through.

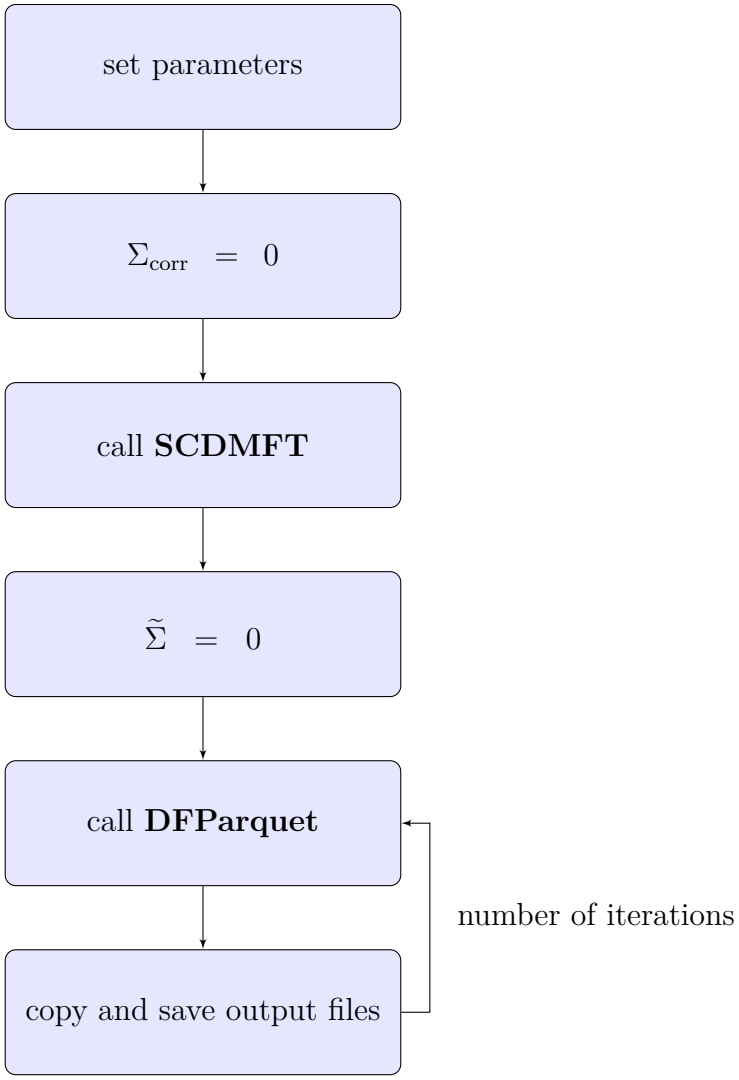

Figure A.1 – Flow diagram of the Python code used for the parquet DF implementation. After setting the parameters and Σ_{corr}=0, the module **SCDMFT** is called to execute a DMFT self-consistent cycle for the FKM. The dual self-energy $\widetilde{\Sigma}$ is set to zero, before the module **DFParquet** is called using the DMFT results as input. **DFParquet** is called according to the number of iterations specified, in each step the output files of it are copied and saved.

References

[1] P. Hohenberg and W. Kohn. Inhomogeneous electron gas. Phys. Rev. **136**, B864 (1964).

[2] N. F. Mott. Metal-insulator transition. Rev. Mod. Phys. **40**, 677, (1968).

[3] J. G. Bednorz and K. A. Müller. Possible high T_c superconductivity in the Ba- La-Cu-O system. Zeitschrift für Physik B Condensed Matter **64**, 189–193 (1986).

[4] J. Hubbard. Electron correlations in narrow energy bands. Proc. R. Soc. Lond. A **276**, 238–257 (1963).

[5] L. M. Falicov and J. C. Kimball. Simple model for Semiconductor-Metal Transitions: SmB_6 and Transition-Metal Oxides. Phys. Rev. Lett. **22**, 997 (1969).

[6] W. Metzner and D. Vollhardt. Correlated lattice fermions in d=∞ dimensions. Phys. Rev. Lett. **62**, 324 (1989).

[7] A. Toschi, A. A. Katanin, and K. Held. Dynamical vertex approximation: A step beyond dynamical mean-field theory. Phys. Rev. B **75**, 045118 (2007).

[8] A. N. Rubtsov, M. I. Katsnelson, and A. I. Lichtenstein. Dual fermion approach to nonlocal correlations in the Hubbard model. Phys. Rev. B **77**, 033101 (2008).

[9] A. Kauch, P. Pudleiner, K. Astleithner, T. Ribic, and K. Held. π-ton – generic optical excitation of correlated systems. arXiv e-prints arXiv:1902.09342 (2019).

[10] A. M. Zagoskin. *Quantum theory of many-body systems.* (Springer, 1998).

[11] P. Coleman. *Introduction to Many-Body Physics.* (Cambridge University Press, 2015).

[12] R. Kubo. Statistical mechanical theory of irreversible processes. i: general theory and simple applications to magnetic and conduction problems. Journal of the Physical Society of Japan **12**, 570–586 (1957).

[13] G. Rohringer, H. Hafermann, A. Toschi, A. A. Katanin, A. E. Antipov, M. I. Katsnelson, A. I. Lichtenstein, A. N. Rubtsov, and K. Held. Diagrammatic routes to nonlocal correlations beyond dynamical mean field theory. Rev. Mod. Phys. **90**, 025003 (2018).

[14] A. Georges and G. Kotliar. Hubbard model in infinite dimensions. Phys. Rev. B **45**, 6479 (1992).

[15] A. Altland and B. D. Simons. *Condensed matter field theory.* (Cambridge University Press, 2010).

[16] T. Ribic, G. Rohringer, and K. Held. Local correlation functions of arbitrary order for the Falicov-Kimball model. Phys. Rev. B **95**, 155130 (2017).

[17] T. Ribic, P. Gunacker, S. Iskakov, M. Wallerberger, G. Rohringer, A. N. Rubtsov, E. Gull, and K. Held. Role of three-particle vertex within dual fermion calculations. Phys. Rev. B **96**, 235127 (2017).

[18] A. A. Katanin. The effect of six-point one-particle reducible local interactions in the dual fermion approach. Journal of Physics A: Mathematical and Theoretical **46**, 045002 (2013).

[19] J. K. Freericks and V. Zlatić. Exact dynamical mean-field theory of the Falicov-Kimball model. Rev. Mod. Phys. **75**, 1333 (2003).

[20] T. Ribic, G. Rohringer, and K. Held. Nonlocal correlations and spectral properties of the Falicov-Kimball model. Phys. Rev. B **93**, 195105 (2016).

[21] A. E. Antipov, E. Gull, and S. Kirchner. Critical exponents of strongly correlated fermion systems from diagrammatic multiscale methods. Phys. Rev. Lett. **112**, 226401 (2014).

[22] S.-X. Yang, P. Haase, H. Terletska, Z. Y. Meng, T. Pruschke, J. Moreno, and M. Jarrell. Dual-fermion approach to interacting disordered fermion systems. Phys. Rev. B **89**, 195116 (2014).

[23] M. Jarrell and J. E. Gubernatis. Bayesian inference and the analytic continuation of imaginary-time quantum monte carlo data. Physics Reports **269**, 133–195 (1996).

[24] D. Geffroy, J. Kaufmann, A. Hariki, P. Gunacker, A. Hausoel, and J. Kunes. Collective modes in ordered mott systems: dynamical mean-field study. arXiv e-prints arXiv:1808.08046 (2018).

[25] J. Frenkel. On the transformation of light into heat in solids. i. Phys. Rev. **37**, 17 (1931).

[26] G. H. Wannier. The structure of electronic excitation levels in insulating crystals. Phys. Rev. **52**, 191 (1937).

[27] B. L. Altshuler and A. G. Aronov. *Electron–electron interaction in disordered conductors,* edited by A. I. Efros and M. Pollak. (Elsevier Science Publisher, 1985).

[28] S. Iskakov, A. E. Antipov, and E. Gull. Diagrammatic monte carlo for dual fermions. Phys. Rev. B **94**, 035102 (2016).

[29] https://github.com/adepttin/fk-fga-.